

See discussions, stats, and author profiles for this publication at: <https://www.researchgate.net/publication/329951779>

# The CMG Helicase Bypasses DNA-Protein Cross-Links to Facilitate Their Repair

Article in *Cell* · December 2018

DOI: 10.1016/j.cell.2018.10.053

CITATIONS

20

READS

96

8 authors, including:



**Justin Sparks**

Harvard Medical School

17 PUBLICATIONS 360 CITATIONS

[SEE PROFILE](#)



**Gheorghe Chistol**

Stanford University

13 PUBLICATIONS 360 CITATIONS

[SEE PROFILE](#)



**Markus Räschle**

Max Planck Institute of Biochemistry

30 PUBLICATIONS 1,980 CITATIONS

[SEE PROFILE](#)



**Nicolai Balle Larsen**

University of Copenhagen

23 PUBLICATIONS 421 CITATIONS

[SEE PROFILE](#)

Some of the authors of this publication are also working on these related projects:



Mismatch Repair [View project](#)



Undergraduate Thesis [View project](#)

# **The CMG helicase bypasses DNA-protein cross-links to facilitate their repair**

Justin L. Sparks<sup>1,6</sup>, Gheorghe Chistol<sup>1,6</sup>, Alan O. Gao<sup>1,2</sup>, Markus Räschle<sup>3</sup>, Nicolai B. Larsen<sup>2</sup>,  
Matthias Mann<sup>2,4</sup>, Julien P. Duxin<sup>2</sup>, and Johannes C. Walter<sup>1,5,#,\*</sup>

<sup>1</sup>Department of Biological Chemistry and Molecular Pharmacology,  
Harvard Medical School, Boston, MA 02115, USA

<sup>2</sup>Novo Nordisk Foundation Center for Protein Research, Faculty of Health and Medical Sciences, University of  
Copenhagen, DK-2200 Copenhagen, Denmark

<sup>3</sup>Department of Molecular Biotechnology and Systems Biology, Technical University of Kaiserslautern, 67653  
Kaiserslautern, Germany

<sup>4</sup>Department of Proteomics and Signal Transduction, Max Planck Institute of Biochemistry, 82152 Martinsried,  
Germany

<sup>5</sup>Howard Hughes Medical Institute

<sup>6</sup>These authors contributed equally

#Lead Contact

\*Correspondence: [johannes\\_walter@hms.harvard.edu](mailto:johannes_walter@hms.harvard.edu)

## Summary

Covalent DNA-protein cross-links (DPCs) impede replication fork progression and threaten genome integrity. Using *Xenopus laevis* egg extracts, we previously showed that when a replication fork encounters a DPC, the DPC is degraded to a short peptide, followed by translesion DNA synthesis. We show here that when DPC proteolysis is blocked, the replicative DNA helicase CMG (CDC45, MCM2-7, GINS), which travels on the leading strand template, bypasses an intact leading strand DPC. Single molecule imaging reveals that GINS does not dissociate from CMG during bypass and that CMG slows dramatically after bypass, likely due to uncoupling from the stalled leading strand. The DNA helicase RTEL1 facilitates bypass, apparently by generating single-stranded DNA downstream of the DPC. The absence of RTEL1 impairs DPC proteolysis, suggesting that CMG must bypass the DPC prior to proteolysis. Our results provide a potential mechanism to prevent inadvertent CMG destruction by DPC proteases, and they reveal CMG's remarkable capacity to overcome obstacles on its translocation strand.

## Introduction

DNA replication forks encounter numerous obstacles that challenge genome duplication. Discrete DNA lesions (e.g. pyrimidine dimers) generally stall the replicative DNA polymerase but not the helicase, leading to helicase-polymerase uncoupling (Byun et al., 2005; Taylor and Yeeles, 2018). How the eukaryotic helicase behaves after uncoupling is unknown, but data from prokaryotes suggests that uncoupled helicases unwind DNA slowly (Graham et al., 2017; Kim et al., 1996; Stano et al., 2005). Bulkier obstacles also block the replicative DNA helicase and therefore stall the entire replisome. These include DNA interstrand cross-links (ICLs; (Fu et al., 2011)) and DNA protein cross-links (DPCs; (Duxin et al., 2014)), in which a protein is covalently linked to one strand of the DNA. DPCs are formed by exogenous agents such as ultraviolet light and ionizing radiation, as well as the chemotherapeutics cisplatin, mitomycin C, and nitrogen mustard (Ide et al., 2011; Stingle et al., 2017; Vaz et al., 2017). DPCs are also generated by endogenous agents such as formaldehyde, abasic sites, reactive oxygen species, and topoisomerases. In addition to ICLs and DPCs, proteins that are tightly bound to DNA interfere with replication fork progression. These non-covalent nucleoprotein complexes include RNA polymerases, tightly bound transcription factors, centromeric chromatin, and pre-replication complexes.

Recent studies have greatly advanced our understanding of how eukaryotic organisms repair covalent DPCs. DPCs smaller than ~8 kD can be excised by nucleotide excision repair whereas larger DPCs require more complex pathways (Ide et al., 2011). While some studies proposed that the response to large DPCs involves strand breakage and recombination, this idea has been challenged (Rosado et al., 2011). In 2014, Wss1 was identified as a DNA-dependent protease that degrades DPCs in yeast, and genetic experiments suggested it operates in S phase (Stingle et al., 2014). Contemporaneous experiments in *Xenopus laevis* egg extracts showed that when a replication fork collides with a DPC on the leading (DPC<sup>Lead</sup>)

or lagging strand template (DPC<sup>Lag</sup>), the DPC undergoes proteolysis by an unknown protease, leaving behind a short peptide adduct that is bypassed by translesion DNA polymerases (Figure 1A) (Duxin et al., 2014). Together, these studies established the existence of a protease-mediated DPC repair pathway that does not involve a double-strand break intermediate or recombination.

Like Wss1, its vertebrate ortholog SPRTN (also named Spartan or DVC1) is a DNA-dependent protease (Lopez-Mosqueda et al., 2016; Morocz et al., 2017; Stingele et al., 2016; Vaz et al., 2016). In mammalian cells expressing protease-deficient SPRTN, DPCs accumulate on chromatin, replication fork progression is impaired, and DNA damage and genome instability are observed (Lessel et al., 2014; Maskey et al., 2017; Maskey et al., 2014; Vaz et al., 2016). In humans, mutations in SPRTN's protease domain cause Ruijs-Aalfs syndrome (RJALS), a human genetic disease characterized by genome instability, premature aging, and early onset liver cancer (Lessel et al., 2014). Collectively, these experiments suggest that SPRTN suppresses cell death, liver cancer, and aging by removing DPCs that block replication fork progression. In frog egg extracts, SPRTN and the proteasome have overlapping functions in promoting replication-coupled DPC proteolysis (Larsen et al., *submitted*; manuscript enclosed). In this system, SPRTN activity requires that a nascent strand be extended to within a few nucleotides of the DPC, whereas proteasome activity requires DPC ubiquitylation and the presence of ssDNA near the adduct. A central, unanswered question is how a DPC is selectively degraded without concomitant destruction of the neighboring, stalled replisome, which would cause fork collapse and genome instability.

The replicative DNA helicase is the first component of the replisome to encounter nucleoprotein complexes on the DNA template, and understanding how the helicase overcomes such obstacles is critical. Replicative helicases form hexameric rings that translocate along one of the two template strands, leading to DNA unwinding ("steric

exclusion”)(O'Donnell and Li, 2018). The bacterial replicative DnaB helicase, which translocates with 5' to 3' polarity along the lagging strand template, stalls when it encounters non-covalent nucleoprotein complexes. To overcome these obstacles, it employs two accessory helicases, UvrD and Rep, which act redundantly (Guy et al., 2009). As 3' to 5' helicases, Rep and UvrD assemble on the leading strand template and likely cooperate with DnaB in overcoming obstacles.

In contrast to DnaB, the eukaryotic replicative DNA helicase, CMG (a complex of CDC45, MCM2-7, and GINS), encircles and translocates 3' to 5' along the leading strand template (Fu et al., 2011). While purified CMG stalls at a biotin-streptavidin (SA) complex on the lagging strand template, MCM10 helps overcome the barrier (Langston and O'Donnell, 2017; Langston et al., 2017). In contrast, MCM10 does not promote CMG bypass of a leading strand biotin-SA complex, suggesting that CMG alone cannot translocate past a bulky leading strand adduct ((Langston et al., 2017) see also (Nakano et al., 2013)). Interestingly, the large T antigen DNA helicase can bypass a DPC on the translocation strand, perhaps via transient ring-opening (Yardimci et al., 2012b). Whether CMG progression past covalent or non-covalent nucleoprotein complexes is assisted by accessory helicases, as seen in bacteria, has not been directly examined. However, consistent with this idea, the 5' to 3' helicases Rrm3 and Pif1 help replication fork progression past non-covalent nucleoprotein complexes in yeast (Ivessa et al., 2000). These results suggest that, like bacteria, yeast cells overcome obstacles by engaging an accessory DNA helicase that moves on the strand opposite the one hosting CMG.

Based on experiments in *Xenopus* egg extracts, we previously proposed that DPC proteolysis allows the CMG helicase to move past DPC<sup>Lead</sup> (Figure 1A)(Duxin et al., 2014). We now show that CMG can bypass DPC<sup>Lead</sup> in the absence of DPC proteolysis. Single-molecule imaging demonstrates that GINS does not dissociate during bypass and that CMG slows dramatically after bypass, likely due to temporary uncoupling from the leading strand, which

stalls at the DPC. The 5' to 3' helicase RTEL1 facilitates CMG bypass of the DPC, and bypass is required for efficient DPC proteolysis. This “bypass first” mechanism is expected to help prevent CMG proteolysis, which would cause replication fork collapse. RTEL1 also promotes fork progression through an array of Lac repressor molecules bound non-covalently to DNA. Our data show that, in conjunction with an accessory helicase, CMG exhibits a remarkable capacity to overcome formidable nucleoprotein obstacles.

## Results

### Leading strands rapidly approach a non-degradable DPC

To study the mechanism of DPC repair, we incubated the 45 kDa DNA methyltransferase M.HpaII with a plasmid containing a fluorinated M.HpaII recognition site (CCGG), which leads to covalent trapping of the enzyme on DNA (Figure S1A; (Chen et al., 1991; Duxin et al., 2014)). We previously showed that when this plasmid (pDPC) is replicated in *Xenopus* egg extracts, leading strands stall 30 nucleotides (nt) from the adducted base due to the footprint of the CMG helicase, which translocates along the leading strand template (Figure 1A; (Duxin et al., 2014)). After a short pause, synthesis resumes and nascent leading strands approach to within 1 nucleotide of the DPC (“approach”), followed by translesion DNA synthesis by the REV1-DNA pol  $\zeta$  complex (Figure 1A, (Duxin et al., 2014)). Because degradation of the DPC roughly coincides with the disappearance of the 30 nt CMG footprint, the results suggested that degradation of the DPC allows CMG to move beyond the adduct (Duxin et al., 2014)(Figure 1A). Surprisingly, however, when DPC proteolysis was blocked via ubiquitin depletion (by supplementing extracts with the de-ubiquitylating enzyme inhibitor Ub-VS), the nascent leading strand still approached the adduct, albeit very inefficiently, suggesting that CMG eventually vacates its position in front of the DPC (Figure 1B; (Duxin et al., 2014)). Moreover, the nascent lagging strand was ultimately extended beyond the DPC. These results show that the replication fork can eventually move past an intact DPC, but the fate of CMG in this process was unclear (Figure 1B).

Given the importance of ubiquitin signaling in the DNA damage response, we wanted to block degradation of the DPC without ubiquitin depletion and examine the effect on approach. To this end, we took advantage of the fact that the DPC is degraded in egg extracts by two overlapping, replication-coupled pathways (Figure S1B; Larsen et al., *submitted*, manuscript enclosed). In one pathway, arrival of the leading strand at the DPC stimulates DPC proteolysis

by SPRTN. In the other pathway, ubiquitylation of the DPC promotes its destruction by the proteasome. To inhibit the SPRTN pathway, we used egg extracts immunodepleted of SPRTN (Figure S1C); to inhibit the proteasome pathway, we employed a DPC whose lysine residues had been chemically methylated to prevent ubiquitylation (meDPC; Figure 1C, spheres with bold outlines). Under these conditions, the DPC was not degraded, and we refer to this as a “stable” DPC (Figure S1D, lanes 7-11; (Larsen et al., *submitted*)). To ensure that a single fork encountered the stable DPC on the leading strand template (“DPC<sup>Lead</sup>”), we flanked the meDPC on the right with 48 tandem copies of *lacO* bound by the Lac repressor (LacR), which blocks arrival of the leftward, converging fork (see grey inset in Figure 1C; (Duxin et al., 2014)). To monitor progress of the rightward leading strand, we digested the DNA with AatII and FspI (Figure 1C; grey inset). Strikingly, the 30 nt CMG footprint disappeared with the same kinetics whether or not proteolysis occurred (Figure 1C; compare lanes 1-6 and 7-12, lower autoradiogram; see graph for quantification). The staggered cuts made by AatII also distinguish leading and lagging strand extension products (Figure 1C; grey inset, pink and purple arrows), which revealed that the lagging strand was readily extended past the stable DPC (Figure 1C, lanes 7-12, top autoradiogram). Leading strand extension past DPC<sup>Lead</sup> was much slower than lagging strand extension (Figure 1C, lanes 1-6), and the former was further delayed when the DPC was stabilized (Figure 1C, lanes 1-12). Leading strand extension past the stable DPC<sup>Lead</sup> was strongly inhibited by Rev1 depletion, demonstrating a requirement for TLS (Figure S1E). Collectively, these results show that when ubiquitin levels are normal, the CMG footprint disappears from the DPC and the lagging strand is extended past the DPC with the same kinetics whether or not the DPC undergoes proteolysis. There are two possible interpretations of this result. First, upon fork stalling, CMG rapidly dissociates from chromatin, allowing leading strand approach to the lesion without DPC proteolysis (Figure S1Fi). In this scenario, a helicase other than CMG unwinds DNA past the DPC to allow lagging strand

extension. Second, CMG normally bypasses the DPC before its destruction, in which case leading strand approach to the lesion and lagging strand extension past the lesion do not require DPC proteolysis (Figure S1Fii).

### **CMG bypasses a stable DPC**

To address whether CMG dissociates from or translocates past a stable DPC<sup>Lead</sup>, we examined approach in the presence of an inhibitor of the p97 ATPase (p97i), which is required to extract CMG from chromatin during replication termination and ICL repair (Dewar et al., 2017; Fullbright et al., 2016; Maric et al., 2014; Moreno et al., 2014; Semlow et al., 2016). If CMG has to dissociate from the stalled replisome to enable approach, p97i should delay approach; if CMG bypasses the DPC to enable approach and dissociates only later, p97i should have no effect. As shown in Figure 1C, p97i did not slow the kinetics of leading strand approach to or lagging strand extension past a stable DPC (compare lanes 7-12 and 19-24, lower radiogram; see graph for quantification). To directly examine the fate of CMG after DPC encounter and how this is affected by p97i, we monitored CMG binding to the plasmid pmeDPC<sup>2xLead</sup> in SPRTN-depleted extract, where both converging CMGs encounter a stable DPC on the leading strand template (Figure 1D; cartoon). The data show that p97i blocked unloading of CMGs from a DPC-containing plasmid. However, given that the kinetics with which the CMG footprint disappeared at a stable DPC was unaffected by p97i (Figure 1C), CMG must have bypassed the DPC. We infer that the CMG unloading observed in the absence of p97i occurs after CMG bypass, convergence with another CMG, and removal via the mechanism employed during replication termination (Figure S1G; (Dewar et al., 2015; Dewar et al., 2017)). DPC bypass was not affected when an inhibitor of CDC7 kinase was added immediately after forks had reached the DPC, indicating that bypass does not involve new origin firing downstream of the DPC (Figure S1H). Bypass was not inhibited by

immunodepletion of the FANCM ATPase (Figure S1I-J), which blocks FANCD2 ubiquitylation (data not shown), or inhibition of ATR signaling (Figure S1K), suggesting bypass is mechanistically distinct from replication fork traverse of DNA interstrand cross-links (Huang et al., 2013; Ling et al., 2016). Together, our data strongly support the idea that CMG bypasses a bulky DPC on the translocation strand.

### **ssDNA downstream of a stable DPC facilitates CMG bypass**

Inspired by work in bacteria (Guy et al., 2009), we speculated that a 5' to 3' accessory helicase might load onto the lagging strand template and assist CMG bypass of a leading strand DPC (Figure S2i). As an initial test of this idea, we placed a second meDPC on the lagging strand template 15 nt upstream of the leading strand DPC (pmeDPC<sup>Lag/Lead</sup>), as this might block unwinding by a 5' to 3' helicase (Figure S2ii). We also placed the second DPC 15 nt downstream of the leading strand DPC (pmeDPC<sup>Lead/Lag</sup>), reasoning that this would allow some DNA unwinding beyond the DPC by an accessory helicase, which might be sufficient to promote bypass (Figure S2iii). Consistent with the action of a 5' to 3' helicase, CMG bypass (as measured via disappearance of the CMG footprint) was severely inhibited by the upstream but not the downstream lagging strand DPC (Figure 2, lanes 19-24 vs. 25-30; graph for quantification). This model further predicts that a ssDNA bubble placed immediately downstream of the DPC should rescue CMG bypass on pmeDPC<sup>Lag/Lead</sup> (Figure S2iv; pmeDPC<sup>Lag/Lead-Bubble</sup>). Since there are only 4 bp between the DPC attachment site and the bubble, arrival of CMG should be sufficient to melt the duplex surrounding the DPC (Figure S2iv). As shown in Figure 2 (lanes 31-36), a 40 nt ssDNA bubble fully rescued bypass in the presence of the upstream DPC<sup>Lag</sup>. Remarkably, bypass was now even faster than on the DNA template lacking any lagging strand obstruction (Figure 2, compare lanes 31-36 with lanes 7-12; see graph for quantification). Interestingly, two tandem meDPCs placed 15 nucleotides

apart on the leading strand template also severely impaired bypass (Figure 2, lanes 13-18; see graph for quantification), suggesting that a single CMG cannot simultaneously accommodate two closely spaced DPCs during bypass. Together, the data suggest that generation of ssDNA downstream of the lesion is rate-limiting for CMG bypass of DPC<sup>Lead</sup>, consistent with assistance by a 5' to 3' helicase.

### **RTEL1 promotes efficient CMG bypass of a stable DPC**

Vertebrates contain at least six 5' to 3' DNA helicases (RTEL1, FANCI, PIF1, DDX3, DDX11, and XPD). Using plasmid pull-down combined with mass spectrometry (PP-MS), all of these helicases except DDX11 were detected on chromatin in egg extracts (Figure 3A; (Larsen et al., *submitted*)). Some bound in a replication-dependent fashion (PIF1, RTEL1, and FANCI), and one (DDX3) was enriched on pDPC. Depletion of PIF1, FANCI, or DDX3 had no significant effects on bypass of a stable DPC<sup>Lead</sup> (data not shown; we did not examine XPD or DDX11). In contrast, immunodepletion of RTEL1 (Figure 3B; see Figure S3A for explanation of RTEL1 isoforms in lane 1 of Figure 3B) caused leading strands to initially stall at a greater distance from the stable DPC<sup>Lead</sup> (Figure 3C, -38 to -44 cluster) and greatly delayed their approach to the adduct (Figure 3C; see graph for quantification). Furthermore, RTEL1 depletion delayed the advance of the lagging strand beyond DPC<sup>Lead</sup> (Figure 3D, lanes 6-10, upper autoradiogram). These results indicate that RTEL1 is required for efficient CMG bypass and that bypass allows new Okazaki fragment priming downstream of the adduct. RTEL1 depletion had no effect on the overall efficiency of DNA synthesis (Figure S3B). The defect in CMG bypass was rescued by wild type recombinant RTEL1 but not by an ATPase deficient RTEL1 mutant (RTEL1<sup>K48R</sup>), which further inhibited bypass (Figure 3C; Figure S3C). Importantly, RTEL1 depletion had only a modest effect on bypass when a single-stranded DNA bubble was placed downstream of the DPC, and it did not further inhibit bypass when meDPC<sup>Lag</sup> was

present upstream (Figure S3D; see graph for quantification). Collectively, these data indicate that RTEL1 enables efficient CMG bypass of intact DPC<sup>Lead</sup>, primarily by generating a short patch of ssDNA near the adduct. The residual bypass observed in RTEL1-depleted extracts (Figure 3C) could be due to incomplete RTEL1 depletion, the presence of partially compensating accessory helicases, or bypass that is independent of accessory helicases.

We speculated that in the absence of RTEL1, a converging fork might generate the single-stranded DNA needed for bypass. Indeed, we found that the bypass defect observed when a single fork collided with DPC<sup>Lead</sup> in RTEL1-depleted egg extract was rescued by the addition of IPTG, which disrupted the LacR array and allowed a second fork to converge on the DPC (Figure 3E, lanes 18-22 vs. 23-28; see graph for quantification). This rescue was not due to CMG unloading as it still occurred in the presence of p97i (Figure 3E, lanes 23-28 vs. 29-34). Our data supports a model in which DPC bypass requires ssDNA beyond the adduct, which can be created by an accessory helicase like RTEL1 or a converging replication fork.

The structures of DNA methyltransferases bound to DNA (Klimasauskas et al., 1994; Reinisch et al., 1995) suggest that M.HpaII interacts intimately with both strands of the double helix. Therefore, covalent coupling of M.HpaII to one strand is expected to hyperstabilize the underlying DNA duplex. To test whether RTEL1 helps disrupt such a hyperstable duplex, we examined DPC<sup>Lag</sup>, which should stabilize the underlying DNA without blocking the translocation strand. As shown in Figure 3D, RTEL1 depletion delayed bypass of DPC<sup>Lag</sup>, but the delay was less pronounced than at DPC<sup>Lead</sup> (Figure 3D and Figure S3E). Collectively, these observations suggest that RTEL1 not only helps CMG disrupt hyperstable DNA duplex but also to overcome obstacles that are covalently attached to CMG's translocation strand.

### **Efficient DPC proteolysis requires RTEL1**

As shown in Figure 1C, the kinetics of CMG bypass were identical whether or not the DPC was degraded. This observation strongly implies that CMG normally bypasses the DPC before proteolysis, and it raised the question of whether bypass might be a pre-requisite for proteolysis. To address this, we replicated a plasmid containing non-methylated DPC<sup>Lead</sup> in undepleted extract so that both proteolysis pathways were active. The extract was either mock-depleted or depleted of RTEL1. At different times, we isolated the plasmid under stringent conditions so that only M.HpaII that was covalently attached to DNA was recovered. After DNA digestion, immunoblotting revealed M.HpaII polyubiquitylation, followed by a decline in M.HpaII levels, which reflects replication-dependent proteolysis (Figure 4A, lanes 1-6; Larsen et al., *submitted*). Strikingly, M.HpaII degradation was delayed by 15-20 min in extracts depleted of RTEL1 (Figure 4A, lanes 7-12). This defect was rescued by wild type RTEL1 but not the ATPase mutant (Figure 4A, lanes 13-24; see graph for quantification). RTEL1 was required for efficient CMG bypass even when the DPC could be degraded, consistent with CMG bypass normally preceding DPC proteolysis (Figure 4B). In the absence of RTEL1, M.HpaII proteolysis was delayed but not eliminated (Figure 4A), and this can be explained by the substantial CMG bypass that still occurred in these conditions (Figure 4B), either due to incomplete RTEL1 depletion, other partially compensating 5' to 3' DNA helicases, or bypass that is independent of accessory helicases. Together, the data indicate that RTEL1-mediated unwinding past the DPC is essential for its efficient proteolysis.

### **RTEL1-dependent DPC bypass promotes SPRTN activity**

To examine whether RTEL1 is required for the SPRTN proteolysis pathway, we examined meDPC, which cannot be ubiquitylated and therefore is not susceptible to the proteasome but can still be degraded by SPRTN (Larsen et al., *submitted*). The action of SPRTN was visible from the appearance of a specific M.HpaII degradation fragment that was absent in  $\Delta$ SPRTN

extract (Figure 4C; lanes 1-10; Larsen et al., *submitted*). In the absence of RTEL1, accumulation of the SPRTN-specific fragment was delayed (Figure 4C; compare lanes 1-5 and 11-15). As seen for DPC bypass, these defects were rescued by wild type but not ATPase deficient RTEL1 (Figure 4C, lanes 16-25), indicating that DNA unwinding past the DPC by RTEL1 is required for SPRTN activity. To address whether CMG bypass itself is required, we examined the effect of tandem leading strand meDPCs since these severely impair CMG bypass (Figure 2, lanes 13-18), presumably without affecting RTEL1's ability to unwind past the adducts. As shown in Figure 4D, tandem meDPCs severely inhibited the appearance of the SPRTN-specific M.HpaII fragment compared to single meDPCs, which allow CMG bypass. Our data indicate that RTEL1-dependent DNA unwinding and CMG bypass of the DPC are both required for the SPRTN pathway.

We next addressed whether RTEL1 affects the proteasome pathway. A detailed time course revealed that in the absence of RTEL1, the appearance of highly ubiquitylated M.HpaII species was delayed, suggesting that RTEL1 is required for efficient DPC ubiquitylation (Figure 4E). To specifically examine the effect of RTEL1 on the proteasome pathway, we replicated pDPC<sup>2xLeads</sup> in SPRTN depleted-extract with or without additional RTEL1 depletion and examined DPC proteolysis, using MG262 addition as a positive control for proteasome inhibition. As shown in Figure 4F, RTEL1 depletion stabilized M.HpaII to a similar extent as MG262 in  $\Delta$ SPRTN extract (compare lanes 11-15 with 16-20), consistent with RTEL1 functioning in the proteasome pathway. Finally, in RTEL1-depleted extracts, chromatin-binding of SPRTN was reduced, and binding of the PSA3 proteasome subunit was delayed (Figure S4A). Together, our experiments indicate that RTEL1 is required for both proteolysis pathways.

Although the requirement for RTEL1's ATPase activity in DPC proteolysis strongly argues it functions by unwinding DNA at the DPC, we wanted to address whether it also plays a more direct role, for example by recruiting one or both proteases. To address this possibility,

we exploited the fact that a ssDNA gap across from the DPC stimulates DPC proteolysis by SPRTN and the proteasome in the absence of a replication fork, obviating the need for CMG bypass or DNA unwinding at the DPC (Figure S4C, lanes 1-6; Larsen et al., *submitted*). Importantly, RTEL1 depletion had no effect on DPC ubiquitylation or proteolysis in this replication-independent setting (Figure S4C, lanes 7-12). Similarly, production of the SPRTN degradation fragment from meDPC placed in a ssDNA gap did not depend on RTEL1 (Figure S4D). These data show that in the presence of ssDNA, RTEL1 is not required for SPRTN activity or overall DPC proteolysis, further indicating that the primary function of RTEL1 is to unwind DNA around the adduct.

### **Direct observation of DPC bypass by single molecule analysis**

To investigate CMG dynamics during DNA replication and DPC repair in *Xenopus* egg extracts, we developed a single-molecule assay called KEHRMIT (Kinetics of the Ekaryotic Helicase by Real-time Molecular Imaging and Tracking) that is similar to a previous approach developed in yeast extracts (Duzdevich et al., 2015). DNA replication was initiated in a microfluidic flow cell on stretched  $\lambda$  DNA (48.5 kb) (Figure 5Ai-iii) using GINS-depleted egg extract reconstituted with active, recombinant GINS labeled on its Psf3 subunit with Alexa Fluor 647 (Figure 5B, Figure S5A-D; rGINS<sup>AF647</sup> labeling efficiency  $\geq 90\%$ ). After ~2 minutes, when only a few origins per  $\lambda$  DNA had fired, we flowed in GINS-depleted extract lacking rGINS<sup>AF647</sup> to prevent further origin firing and to remove background fluorescence (Figure 5Aiv). Subsequent imaging of AF647 (Figure 5Av) revealed that each replication origin gave rise to two diffraction-limited spots of comparable intensity that traveled in opposite directions (Figure 5C, green). Spots photobleached in a single step, indicating they contain a single rGINS<sup>AF647</sup> molecule (Figure S5E). CMGs travelled at an average velocity of ~400 nt per min (Figure 5D), consistent with replication fork rates on immobilized DNA templates (Loveland et al., 2012; Yardimci et al.,

2010). Furthermore, rGINS<sup>AF647</sup> migrated at the leading edge of nascent DNA tracts (Figure 5C, blue; see legend), indicating that each AF647 spot represents a single CMG helicase at a replication fork. Labeled CMG molecules traveled on average 5.3 kilo-bases (kb) before disappearing (Figure 5E). For molecules where the DNA remained attached until the end of the experiment, the nascent DNA tract continued to grow even after loss of AF647 signal (Figure S5F). Given that there is no free pool of GINS during the imaging phase (Figure 5Aiv-v), the loss of AF647 signal reflects photobleaching and not GINS exchange. We conclude that GINS is highly processive and that KEHRMIT is a powerful means to examine CMG dynamics during replication.

To investigate the mechanism of DPC bypass using KEHRMIT, we immobilized a linear DNA substrate containing two site-specific DPCs labeled at their C-termini with Alexa Fluor 568 (AF568) (Figure 6A). If an origin fires between the two lesions, both helicases encounter a DPC<sup>Lead</sup> (Figure 6B, top); otherwise, the inward moving CMG first encounters a DPC<sup>Lag</sup> and then a DPC<sup>Lead</sup> (Figure 6B, bottom). We first conducted KEHRMIT on a meDPC in SPRTN-depleted extract to inhibit DPC proteolysis (Figure S1D; Larsen et al., *submitted*) and thereby maximize the possibility of observing bypass. Strikingly, we saw many instances in which CMG paused at DPC<sup>Lead</sup> and then underwent unambiguous bypass (Figure 6C). Interestingly, CMG slowed down dramatically after bypass, as described below. To objectively identify bypass events and determine how long they take, we applied the following, stringent criteria: (1) both CMG<sup>AF647</sup> and DPC<sup>AF568</sup> signals were present before, during, and after bypass; (2) CMG travelled at least 1-pixel (~500 nt) away from the DPC after bypass; (3) CMG travelled processively for at least 3 time points (3 min) before and after bypass. Based on this automated algorithm, 42-56% of CMGs that encountered meDPC<sup>Lead</sup> in SPRTN-depleted extract bypassed the intact DPC (“BID” events) (Figure 6D, S6A), and CMG paused at meDPC<sup>Lead</sup> for 15 minutes on average before undergoing bypass (Figure 6E). We observed

four other classes of events (Figure 6D, see legend for a detailed description; S6B for examples). Many of these non-BID events probably involve meDPC<sup>Lead</sup> bypass that could not be detected due to the slow rate of CMG progression after bypass, the stringent criteria for BID events, and the premature loss of CMG or DPC signal due to photobleaching (Figure S6C) or DNA breakage. Therefore, the actual DPC<sup>Lead</sup> bypass efficiency was probably substantially higher than 50%. When CMG encountered meDPC<sup>Lag</sup>, it paused on average for only three minutes before moving past the adduct (Figure 6E-F), consistent with ensemble analysis of leading strands (Duxin et al., 2014). In 44-49% of cases, CMG unambiguously bypassed a DPC<sup>Lag</sup> (Figure S6D, BID). In 47-51% of DPC<sup>Lag</sup> encounters, DPC<sup>Lag</sup> became mobile after helicase bypass and then tracked with the bypassed CMG (Figure S6D, B+M; Figure S6E). Since the DNA template is immobilized via 3'-biotin DPC<sup>Lag</sup> probably becomes mobile when the outward moving replisomes reaches the end of the template, which liberates and allows chromatin compaction of the sister chromatid containing the bypassed DPC (Figure S6F). Taking into account BID and B+M events, DPC<sup>Lag</sup> bypass efficiency exceeded 95% (Figure S6D). In conclusion, KEHRMIT shows that CMG efficiently bypasses stable DPC<sup>Lead</sup> and DPC<sup>Lag</sup>, and that this process does not involve GINS dissociation.

To address whether CMG bypasses DPC<sup>Lead</sup> when proteolysis is not impaired, we examined a non-methylated DPC in extract containing SPRTN. As expected, signatures involving early loss of the DPC increased when proteolysis was allowed (Figure 6D; DD- and DD+). In this setting, 11-14% of CMGs exhibited unambiguous DPC<sup>Lead</sup> bypass (Figure 6D; BID). We suspect that many DD+ events represent bona-fide bypass, but failed to meet the BID criteria because DPC proteolysis occurred before CMG traveled far enough beyond the DPC. In support of this hypothesis the probabilities of BID and DD+ events add up to 40-45% for degradable DPC<sup>Lead</sup> – similar to the likelihood of unambiguous bypass (BID 42-56%) for

stabilized DPC<sup>Lead</sup> (Figure 6D). As noted above, any bypass events in the DT, DD-, and CD categories go undetected due to the premature disappearance of DPC and/or CMG signal. Thus, 11-14% is likely a gross underestimate of the true efficiency with which CMG bypassed DPC<sup>Lead</sup>. In conclusion, our results are consistent with the model that CMG bypasses DPC<sup>Lead</sup> prior to proteolytic processing.

### **Differential Kinetics of DPC<sup>Lead</sup> vs. DPC<sup>Lag</sup> Proteolysis**

In our experiments, the AF568 fluorescence signal disappears when the C-terminus of HpaII is degraded, providing a single-molecule measurement of DPC proteolysis. In the absence of replication, virtually no AF568 spots disappeared in the first 10-20min – the time needed for CMG to arrive at a DPC (Figure S6G, + geminin control), demonstrating that AF568 disappearance was due primarily to replication-coupled DPC proteolysis. Importantly, DPC<sup>Lag</sup> fluorescence disappeared ~7 minutes after CMG arrival, whereas DPC<sup>Lead</sup> disappearance took ~25 minutes (Figure 6G). This result is consistent with our finding that proteolysis depends on bypass (Figure 4D) and that bypass takes much longer for DPC<sup>Lead</sup> than DPC<sup>Lag</sup> (Figure 6E). As expected, when the DPC was methylated and examined in SPRTN-depleted extract, both meDPC<sup>Lead</sup> and meDPC<sup>Lag</sup> were greatly stabilized (Figure 6G). In conclusion, the difference between DPC<sup>Lag</sup> and DPC<sup>Lead</sup> destruction is accounted for by the different kinetics with which these lesions are bypassed, supporting the model that bypass is a pre-requisite for proteolysis.

### **CMG slows down after DPC<sup>Lead</sup> bypass**

We investigated how CMG's velocity is affected by collision with DPC<sup>Lead</sup> and DPC<sup>Lag</sup>. Strikingly, while CMG continued moving at 400-500 nt/min after bypassing DPC<sup>Lag</sup>, it slowed to ~80 nt/min after bypassing DPC<sup>Lead</sup> (Figure 6H). We speculated that CMG slowing was due to its uncoupling from leading strand synthesis, which pauses for an extended time when it

reaches DPC<sup>Lead</sup> but not DPC<sup>Lag</sup> (Figure 1C; (Duxin et al., 2014)). To independently assess how CMG uncoupling from the leading strand impacts helicase velocity, we added aphidicolin, a potent inhibitor of replicative polymerases. In the presence of aphidicolin, CMG slowed dramatically (Figure S6H) to an average speed of only ~55 nt/min (Figure 6H). Uncoupled CMGs traveled on average 3.6 kb (Figure S6I) with no detectable pausing. The data strongly imply that the slow rate of CMG translocation after DPC<sup>Lead</sup> bypass is due to CMG uncoupling. In rare instances (3 out of 59 bypass events), we observed that after DPC<sup>Lead</sup> bypass, CMG traveled slowly for several minutes before resuming translocation at a fast rate, indicative of recoupling (Figure 6I). The small number of putative recoupling events is consistent with the low efficiency of TLS after extracts have been depleted, and an apparent absence of efficient repriming by pol $\alpha$  in eukaryotes (Taylor and Yeeles, 2018). Our results suggest that after CMG bypasses DPC<sup>Lead</sup>, CMG uncouples from the leading strand and slows down, minimizing the amount of ssDNA generated while the leading strand undergoes TLS of the peptide adduct.

### **RTEL1 promotes efficient CMG progression past non-covalent nucleoprotein complexes**

As shown in Figure 3D, RTEL1 is required to efficiently bypass a lagging strand DPC, probably because it helps unwind the DNA underlying the DPC. If this interpretation is correct, it follows that RTEL1 should be required for the replicative bypass of any nucleoprotein complex that stabilizes the duplex, even ones that are non-covalent. To address this question, we replicated a plasmid containing an array of 32 *lacO* sites bound by LacR. At different time points, plasmid was recovered and cut with XmnI at a single site before native gel electrophoresis (Figure 7A). We previously showed that in this setting, replication forks converge on the outer edges of the LacR array, generating a discrete X-shaped intermediate whose mobility gradually decreases as forks slowly progress through the array (Figure 7B, lanes 1-6; (Dewar et al., 2015)). When forks meet, the X-shaped species are converted into fully replicated, linear

daughter molecules. As shown in Figure 7B, RTEL1 depletion severely delayed the accumulation of linear molecules (lanes 7-12), and this effect was partially rescued by RTEL1<sup>WT</sup> but not RTEL1<sup>K48R</sup>, which slightly delayed DNA replication (lanes 13-24). To examine fork progression through the LacR array at higher resolution, DNA was nicked near the *lacO* sites with Nt.BspQI, and the radioactive nascent strands were separated on a urea PAGE gel, which reveals fork pausing ~30 nt upstream of each *lacO* site (Figure 5C, lanes 1-6; (Dewar et al., 2015)). Based on this analysis, fork progression through the array was also severely compromised in extracts lacking RTEL1 (Figure 7C, lanes 1-12, red boxes), and the defect was reversed with RTEL1<sup>WT</sup> but not RTEL1<sup>K48R</sup> (Figure 7C, lanes 13-24). Finally, replisome progression does not require proteolysis of LacR as immunodepletion of SPRTN and addition of proteasome inhibitor had no effect on the conversion of X-shaped intermediates to fully replicated daughter molecules (Figure S7A). We conclude that RTEL1 is required to evict non-covalent nucleoprotein complexes and for bypass of DPCs.

## **Discussion**

Our results establish a comprehensive framework to understand how the vertebrate replisome overcomes covalent and non-covalent nucleoprotein obstacles (Figure 7D).

### **Disruption of non-covalent nucleoprotein complexes by RTEL1**

The most common nucleoprotein complexes encountered by replication forks are non-covalent. We showed that CMG progression past a LacR array requires RTEL1, which translocates 5' to 3' on the lagging strand template. Together with prior work in bacteria and yeast (Guy et al., 2009; Ivessa et al., 2000), a conserved mechanism emerges in which replication forks employ an accessory helicase on the strand opposite the one hosting the replicative DNA helicase. In egg extracts and cells, RTEL1 is constitutively associated with replication forks in the absence of experimentally-induced DNA damage (Figure 3A; (Vannier et al., 2013)), suggesting RTEL1 might travel with the replisome. Moreover, RTEL1 appears to be part of a large, CMG-associated replisome progression complex (Dewar et al., 2017), positioning RTEL1 for rapid engagement when obstacles are encountered. RTEL1 probably disrupts non-covalent nucleoprotein complexes by unwinding the underlying DNA, which will, in most cases, displace the protein obstacle from DNA.

### **CMG bypasses DPCs on both strands**

Less commonly, forks will encounter covalent DPCs. We previously showed that the disappearance of the CMG footprint at DPC<sup>Lead</sup> correlates with the latter's proteolysis, and that when DPC<sup>Lead</sup> proteolysis is blocked due to ubiquitin depletion, loss of the footprint is dramatically delayed. On this basis, we proposed that CMG progression past DPC<sup>Lead</sup> requires prior DPC proteolysis (Duxin et al., 2014). However, we now show that when ubiquitin levels are normal, CMG can readily bypass a stable DPC<sup>Lead</sup>. Thus, when DPC proteolysis is blocked

by inhibiting the SPRTN and proteasome pathways, the CMG footprint disappears independently of p97 activity, implying that CMG bypasses the DPC rather than dissociating. In support of this interpretation, single-molecule imaging shows that the same molecule of CMG that encounters a DPC<sup>Lead</sup> also travels past the adduct. Our previous observation that loss of the CMG footprint was inhibited when DPC proteolysis was blocked by a non-specific DUB inhibitor was most likely due to pleiotropic consequences of ubiquitin depletion (Duxin et al., 2014).

We envision two possible mechanisms of DPC<sup>Lead</sup> bypass. In one, CMG threads the denatured DPC through its central channel (Figure S7B). Because most DPCs should be attached to DNA at an internal amino acid, this mechanism would require CMG's central pore to accommodate ssDNA and two polypeptide chains. Notably, the time required for DPC bypass is not influenced by methylation status (Figure S6J compare meDPC vs DPC; Figure 1C for ensemble data), including when MG262 was added to block proteasome activity (Data not shown), suggesting that ubiquitylation of the DPC does not adversely affect bypass. This observation disfavors the "threading" model, which predicts that an ubiquitylated DPC would be much more difficult to accommodate in CMG's central channel, even after it is unfolded. In a second model, the MCM2-7 ring opens, allowing CMG to slide past the DPC (Figure S7C). During licensing, MCM2-7 opens at the MCM2-MCM5 interface to allow dsDNA access to the MCM2-7 central channel (Bochman and Schwacha, 2010; Samel et al., 2014). During initiation, one strand of DNA is ejected from MCM2-7, perhaps through the same MCM2-MCM5 "gate" (Samel et al., 2014). Therefore, MCM2-7 is highly dynamic, and ring opening could plausibly underlie DPC<sup>Lead</sup> bypass. The structure of CMG shows that CDC45 binds on top of the MCM2-5 interface, whereas GINS resides adjacent to it (Abid Ali et al., 2016; Yuan et al., 2016). Therefore, while CDC45 would need to dissociate for the MCM2-5 gate to open, GINS could

remain bound, as seen in our single molecule assays. Future experiments will be required to determine how CMG bypass occurs, and whether it involves CDC45 dissociation.

We recently discovered that upon collision of a replication fork with a DPC, the E3 ubiquitin ligase TRAIIP promotes DPC ubiquitylation and proteolysis (Larsen et al., *submitted*). TRAIIP-dependent DPC ubiquitylation does not require RTEL1 and therefore occurs independently of CMG bypass (Larsen et al., *submitted*). Surprisingly, ubiquitylation of the DPC by TRAIIP appears to contribute to efficient CMG bypass. Given that DPC methylation, which prevents DPC ubiquitylation, does not affect bypass (Figure 1C), we propose that methylation mimics the effect of ubiquitylation on bypass. The role of post-translational modifications in DPC bypass is an important area of future investigation.

It is interesting to consider how RTEL1 might promote bypass. The requirement for RTEL1 in CMG bypass is largely abolished by a converging fork or when a ssDNA bubble is placed downstream of the DPC. These observations suggest that the primary function of RTEL1 is to generate ssDNA downstream of the lesion, which is difficult to reconcile with a model in which CMG denatures the DPC (Figure S7B), as denaturation should not be facilitated by ssDNA downstream. We favor the idea that ssDNA created beyond the DPC allows the breached CMG to re-engage with DNA beyond the DPC. Given that the non-catalytic N-terminal tier of CMG resides at the leading edge of the fork (Douglas et al., 2018; Georgescu et al., 2017), the N-terminus might re-close around ssDNA while the C-terminal ATPase domain is still engaged in bypassing the DPC. According to the “inchworm” mechanism of CMG unwinding, the N-terminal tier of CMG might reach past the DPC when CMG is in the extended conformation (Yuan et al., 2016). Such a mechanism would help avoid accidental dissociation of CMG during DPC bypass.

Although CMG movement past DPC<sup>Lead</sup> and DPC<sup>Lag</sup> both constitute “bypass” events, the underlying mechanisms are different. While CMG pauses briefly at DPC<sup>Lag</sup>, it stalls for an extended period at DPC<sup>Lead</sup>. In addition, the absence of RTEL1 causes greater CMG stalling at DPC<sup>Lead</sup> vs. DPC<sup>Lag</sup>. Given CMG’s translocation along the leading strand template (Fu et al., 2011), these data indicate that the primary role of RTEL1 at DPC<sup>Lag</sup> is to assist CMG in disrupting non-covalent interactions between the DPC and the underlying DNA. In contrast, bypassing a leading strand DPC additionally requires RTEL1-dependent CMG stepping over or around the covalent DPC-DNA linkage. We previously investigated the effect of biotin-streptavidin roadblocks on CMG translocation. Whereas CMG bypass of these obstacles on the lagging strand template takes only 5-10 minutes, the same barriers on the leading strand template stall CMG for ~20-40 minutes (Fu et al., 2011), as seen for DPCs. In summary, although CMG can overcome lagging and leading strand barriers, the latter constitute a more formidable obstacle to the helicase.

### **CMG slows down after uncoupling from the leading strand**

In the presence of DNA damage in the leading strand template, or when DNA synthesis is inhibited, the CMG helicase uncouples from the point of synthesis, leading to the exposure of ssDNA and ATR checkpoint activation (Byun et al., 2005; Taylor and Yeeles, 2018). However, the dynamics of the uncoupled CMG are unknown. We used KEHRMIT to show that in the presence of aphidicolin, the rate of CMG translocation slows 8-fold to ~55 nt/min. Given experiments with prokaryotic DNA helicases (Graham et al., 2017; Kim et al., 1996; Stano et al., 2005), the simplest interpretation of this observation is that optimal CMG activity requires coupling of the helicase with DNA synthesis. Importantly, after CMG bypass of DPC<sup>Lead</sup>, the rate of CMG translocation also slowed dramatically, to about 70-90 nt/min, indicative of CMG uncoupling from the leading strand, which stalls at the DPC. Why a bypassed CMG does not

appear to slow to the same rate observed with aphidicolin is unclear. One possibility is that DPC bypass events are easiest to detect when they involve uncoupled helicases that travel faster than the average. Alternatively, a bypassed CMG might retain helicase co-activators that do not travel with aphidicolin-uncoupled CMG. Either way, slow translocation of the uncoupled CMG limits the amount of ssDNA generated during replication stress. This property of CMGs probably reduces the likelihood of DNA breakage, reduces the time needed for recoupling of the leading strand to CMG after TLS is complete, and may promote template switching by limiting physical separation of the sister chromatids. CMG should slow in response to any insult that induces helicase-leading strand uncoupling, suggesting that CMG slowing probably represents a common response to replication stress.

### **CMG bypass precedes and is required for efficient DPC proteolysis**

The following evidence indicates that CMG bypass precedes and is essential for efficient DPC proteolysis. First, the kinetics of CMG footprint disappearance are unaffected by DPC proteolysis (Figure 1C). This result strongly implies that CMG bypass normally precedes proteolysis. Second, we observe bypass of degradable DPCs in single molecule experiments. Third, when we inhibit CMG bypass (with RTEL1 depletion or tandem DPCs), proteolysis is compromised. Fourth, C-terminal proteolysis takes considerably longer for DPC<sup>Lead</sup> than DPC<sup>Lag</sup>, consistent with the much slower kinetics of DPC<sup>Lead</sup> bypass. Finally, DPC proteolysis by SPRTN requires that the leading strand advance to within a few nucleotides of the DPC (Larsen et al., *submitted*), which is only possible if CMG has moved out of the way. Altogether, the data strongly support the idea that CMG bypass is a pre-requisite for DPC proteolysis.

The relationship between CMG bypass and the proteasome is less clear. RTEL1 depletion appears to impair the production of long ubiquitin chains on the DPC, and it mimics MG262 addition in SPRTN-depleted extracts, implicating RTEL1 in the proteasome pathway.

However, it is unclear whether RTEL1-dependent DNA unwinding at the DPC is sufficient to trigger proteasome activity, or whether CMG bypass is also required. Consistent with the former possibility, ssDNA is sufficient to trigger proteasome-mediated DPC proteolysis in the absence of a leading strand at the lesion (Larsen et al., *submitted*). A mechanism in which proteasome activity requires RTEL1 unwinding but not CMG bypass would allow the destruction of DPCs that cannot be bypassed (e.g. because they are too large).

The “bypass first” mechanism we describe here is well-suited to enhance genome stability. First, CMG movement past DPCs before proteolysis might reduce the probability that the helicase is accidentally destroyed, which is crucial as there is no known pathway to reload MCM2-7 de novo in S phase. Second, if CMG bypass of DPC<sup>Lead</sup> occurs but TLS fails, the lagging strand is still extended past the adduct (Figure 1C; upper autoradiogram). In this case, the leading strand could also be extended past the DPC via template switching (Figure S7D) or re-priming.

### **RTEL1-dependent disruption of nucleoprotein complexes in vivo?**

RTEL1 was first identified as a regulator of telomere homeostasis, and hypomorphic mutations in the human gene cause Hoyeraal-Hreidarsson syndrome, which is characterized by telomere shortening, bone marrow failure, immunodeficiency, and growth retardation (Vannier et al., 2014). RTEL1 promotes telomere homeostasis by resolving telomeric G-quadruplexes and dissolving T-loops, both of which facilitate telomere replication. Interestingly, while homozygous RTEL1 mutations are lethal, deletion of RTEL1’s PIP box leads to defective replication fork progression genome-wide, suggesting that RTEL1 helps overcome endogenous barriers to replication fork progression at non-telomeric loci (Vannier et al., 2013). In egg extracts, the PIP box of RTEL1 is not required to bypass DPCs (data not shown), indicating that *Xenopus* RTEL1 can bind to replication forks via other means. Together, the

evidence is consistent with the possibility that RTEL1 might promote replication fork progression *in vivo* by disrupting covalent and/or non-covalent nucleoprotein complexes. However, the production of ssDNA downstream of a DPC by a converging fork, and possibly by other accessory helicases, appears to be sufficient to promote CMG bypass. Therefore, loss of RTEL1 alone may not cause a detectable bypass defect in cells. Future work will be required to address whether any of the phenotypes observed in RTEL1-deficient mice or humans are attributable to defective bypass of nucleoprotein complexes.

### **Acknowledgements**

We thank Niels Mailand, Peter Burgers, Joe Loparo, and members of the Walter laboratory for feedback on the manuscript. We thank Anna Loveland, Thomas Graham, and Hasan Yardimci for advice regarding single-molecule experiments; Seungwoo Chang for advice regarding sortase labeling and the gift of purified sortase; Benjamin Stinson for advice regarding peptide labeling and purification; and Livio Dukaj for the gift of purified Fen1<sup>mKikGR</sup>. Single-molecule data was collected at the Nikon Imaging Center at Harvard Medical School (NIC@HMS). We are grateful to NIC@HMS staff, especially Jennifer Waters and Talley Lambert, for help configuring the microscope, designing imaging protocols, and a generous allotment of instrument time. J.L.S. is supported by a postdoctoral fellowship from the Damon Runyon Cancer Research Foundation. G.C. was supported by a postdoctoral fellowship from the Jane Coffin Childs Memorial Fund for Medical Research. J.C.W. is supported by NIH grant HL98316. J.C.W. is an investigator of the Howard Hughes Medical Institute. The Novo Nordisk Foundation Center for Protein Research is supported financially by the Novo Nordisk Foundation (Grant agreement NNF14CC0001). J.P.D. received funding from the European Research Council (grant agreement No 715975).

## **Author Contributions**

J.L.S., G.C. and J.C.W. designed and analyzed the experiments and prepared the manuscript. J.L.S. and G.C. performed ensemble and single-molecule experiments, respectively. A.G. developed the protocol to methylate DPCs. G.C. developed the KEHRMIT assay and reagents. M.R. and M.M. performed and analyzed the mass spectrometry. J.P.D. and N.B.L. developed and supplied the pDPC<sup>ssDNA</sup> and pmeDPC<sup>ssDNA</sup> plasmids. J.P.D. developed the stringent plasmid pull-down protocol.

## **Declaration of Interests**

The authors declare no competing interests.

## References

- Abid Ali, F., Renault, L., Gannon, J., Gahlon, H.L., Kotecha, A., Zhou, J.C., Rueda, D., and Costa, A. (2016). Cryo-EM structures of the eukaryotic replicative helicase bound to a translocation substrate. *Nat Commun* 7, 10708.
- Aitken, C.E., Marshall, R.A., and Puglisi, J.D. (2008). An oxygen scavenging system for improvement of dye stability in single-molecule fluorescence experiments. *Biophys J* 94, 1826-1835.
- Arias, E.E., and Walter, J.C. (2005). Replication-dependent destruction of Cdt1 limits DNA replication to a single round per cell cycle in *Xenopus* egg extracts. *Genes Dev* 19, 114-126.
- Bochman, M.L., and Schwacha, A. (2010). The *Saccharomyces cerevisiae* Mcm6/2 and Mcm5/3 ATPase active sites contribute to the function of the putative Mcm2-7 'gate'. *Nucleic Acids Res* 38, 6078-6088.
- Byun, T.S., Pacek, M., Yee, M.C., Walter, J.C., and Cimprich, K.A. (2005). Functional uncoupling of MCM helicase and DNA polymerase activities activates the ATR-dependent checkpoint. *Genes Dev* 19, 1040-1052.
- Chen, I., Dorr, B.M., and Liu, D.R. (2011). A general strategy for the evolution of bond-forming enzymes using yeast display. *Proc Natl Acad Sci U S A* 108, 11399-11404.
- Chen, L., MacMillan, A.M., Chang, W., Ezaz-Nikpay, K., Lane, W.S., and Verdine, G.L. (1991). Direct identification of the active-site nucleophile in a DNA (cytosine-5)-methyltransferase. *Biochemistry* 30, 11018-11025.
- Dewar, J.M., Budzowska, M., and Walter, J.C. (2015). The mechanism of DNA replication termination in vertebrates. *Nature* 525, 345-350.
- Dewar, J.M., Low, E., Mann, M., Raschle, M., and Walter, J.C. (2017). CRL2(Lrr1) promotes unloading of the vertebrate replisome from chromatin during replication termination. *Genes Dev* 31, 275-290.
- Ding, H., Schertzer, M., Wu, X., Gertsenstein, M., Selig, S., Kammori, M., Pourvali, R., Poon, S., Vulto, I., Chavez, E., *et al.* (2004). Regulation of murine telomere length by Rtel: an essential gene encoding a helicase-like protein. *Cell* 117, 873-886.
- Douglas, M.E., Ali, F.A., Costa, A., and Diffley, J.F.X. (2018). The mechanism of eukaryotic CMG helicase activation. *Nature*.
- Duxin, J.P., Dewar, J.M., Yardimci, H., and Walter, J.C. (2014). Repair of a DNA-protein crosslink by replication-coupled proteolysis. *Cell* 159, 346-357.
- Duzdevich, D., Warner, M.D., Ticau, S., Ivica, N.A., Bell, S.P., and Greene, E.C. (2015). The dynamics of eukaryotic replication initiation: origin specificity, licensing, and firing at the single-molecule level. *Mol Cell* 58, 483-494.
- Enoiu, M., Ho, T.V., Long, D.T., Walter, J.C., and Scharer, O.D. (2012). Construction of plasmids containing site-specific DNA interstrand cross-links for biochemical and cell biological studies. *Methods Mol Biol* 920, 203-219.
- Fu, Y.V., Yardimci, H., Long, D.T., Guainazzi, A., Bermudez, V.P., Hurwitz, J., van Oijen, A., Scharer, O.D., and Walter, J.C. (2011). Selective Bypass of a Lagging Strand Roadblock by the Eukaryotic Replicative DNA Helicase. *Cell* 146, 931-941.
- Fullbright, G., Rycenga, H.B., Gruber, J.D., and Long, D.T. (2016). p97 Promotes a Conserved Mechanism of Helicase Unloading during DNA Cross-Link Repair. *Mol Cell Biol* 36, 2983-2994.
- Georgescu, R., Yuan, Z., Bai, L., de Luna Almeida Santos, R., Sun, J., Zhang, D., Yurieva, O., Li, H., and O'Donnell, M.E. (2017). Structure of eukaryotic CMG helicase at a replication fork and implications to replisome architecture and origin initiation. *Proc Natl Acad Sci U S A* 114, E697-E706.
- Graham, J.E., Marians, K.J., and Kowalczykowski, S.C. (2017). Independent and Stochastic Action of DNA Polymerases in the Replisome. *Cell* 169, 1201-1213 e1217.

Guy, C.P., Atkinson, J., Gupta, M.K., Mahdi, A.A., Gwynn, E.J., Rudolph, C.J., Moon, P.B., van Knippenberg, I.C., Cadman, C.J., Dillingham, M.S., *et al.* (2009). Rep provides a second motor at the replisome to promote duplication of protein-bound DNA. *Mol Cell* 36, 654-666.

Habuchi, S., Tsutsui, H., Kochaniak, A.B., Miyawaki, A., and van Oijen, A.M. (2008). mKikGR, a monomeric photoswitchable fluorescent protein. *PLoS One* 3, e3944.

Huang, J., Liu, S., Bellani, M.A., Thazhathveetil, A.K., Ling, C., de Winter, J.P., Wang, Y., Wang, W., and Seidman, M.M. (2013). The DNA Translocase FANCM/MHF Promotes Replication Traverse of DNA Interstrand Crosslinks. *Mol Cell* 52, 434-446.

Ide, H., Shoulkamy, M.I., Nakano, T., Miyamoto-Matsubara, M., and Salem, A.M. (2011). Repair and biochemical effects of DNA-protein crosslinks. *Mutat Res* 711, 113-122.

Ivessa, A.S., Zhou, J.Q., and Zakian, V.A. (2000). The *Saccharomyces* Pif1p DNA helicase and the highly related Rrm3p have opposite effects on replication fork progression in ribosomal DNA. *Cell* 100, 479-489.

Kim, S., Dallmann, H.G., McHenry, C.S., and Marians, K.J. (1996). Coupling of a replicative polymerase and helicase: a tau-DnaB interaction mediates rapid replication fork movement. *Cell* 84, 643-650.

Klimasauskas, S., Kumar, S., Roberts, R.J., and Cheng, X. (1994). HhaI methyltransferase flips its target base out of the DNA helix. *Cell* 76, 357-369.

Langston, L., and O'Donnell, M. (2017). Action of CMG with strand-specific DNA blocks supports an internal unwinding mode for the eukaryotic replicative helicase. *Elife* 6.

Langston, L.D., Mayle, R., Schauer, G.D., Yurieva, O., Zhang, D., Yao, N.Y., Georgescu, R.E., and O'Donnell, M.E. (2017). Mcm10 promotes rapid isomerization of CMG-DNA for replisome bypass of lagging strand DNA blocks. *Elife* 6.

Lebofsky, R., Takahashi, T., and Walter, J.C. (2009). DNA replication in nucleus-free *Xenopus* egg extracts. *Methods Mol Biol* 521, 229-252.

Lebofsky, R., van Oijen, A.M., and Walter, J.C. (2011). DNA is a co-factor for its own replication in *Xenopus* egg extracts. *Nucleic Acids Res* 39, 545-555.

Lessel, D., Vaz, B., Halder, S., Lockhart, P.J., Marinovic-Terzic, I., Lopez-Mosqueda, J., Philipp, M., Sim, J.C., Smith, K.R., Oehler, J., *et al.* (2014). Mutations in SPRTN cause early onset hepatocellular carcinoma, genomic instability and progeroid features. *Nat Genet* 46, 1239-1244.

Lewis, J.S., Spenkelink, L.M., Schauer, G.D., Hill, F.R., Georgescu, R.E., O'Donnell, M.E., and van Oijen, A.M. (2017). Single-molecule visualization of *Saccharomyces cerevisiae* leading-strand synthesis reveals dynamic interaction between MTC and the replisome. *Proc Natl Acad Sci U S A* 114, 10630-10635.

Li, K. (2008). The image stabilizer plugin for ImageJ. [http://www.cscmu.edu/~kangli/code/Image\\_Stabilizer.html](http://www.cscmu.edu/~kangli/code/Image_Stabilizer.html).

Ling, C., Huang, J., Yan, Z., Li, Y., Ohzeki, M., Ishiai, M., Xu, D., Takata, M., Seidman, M., and Wang, W. (2016). Bloom syndrome complex promotes FANCM recruitment to stalled replication forks and facilitates both repair and traverse of DNA interstrand crosslinks. *Cell Discov* 2, 16047.

Lopez-Mosqueda, J., Maddi, K., Prgomet, S., Kalayil, S., Marinovic-Terzic, I., Terzic, J., and Dikic, I. (2016). SPRTN is a mammalian DNA-binding metalloprotease that resolves DNA-protein crosslinks. *Elife* 5.

Loveland, A.B., Habuchi, S., Walter, J.C., and van Oijen, A.M. (2012). A general approach to break the concentration barrier in single-molecule imaging. *Nature methods* 9, 987-992.

Maric, M., Maculins, T., De Piccoli, G., and Labib, K. (2014). Cdc48 and a ubiquitin ligase drive disassembly of the CMG helicase at the end of DNA replication. *Science* 346, 1253596.

Maskey, R.S., Flatten, K.S., Sieben, C.J., Peterson, K.L., Baker, D.J., Nam, H.J., Kim, M.S., Smyrk, T.C., Kojima, Y., Machida, Y., *et al.* (2017). Spartan deficiency causes accumulation of Topoisomerase 1 cleavage complexes and tumorigenesis. *Nucleic Acids Res* 45, 4564-4576.

Maskey, R.S., Kim, M.S., Baker, D.J., Childs, B., Malureanu, L.A., Jeganathan, K.B., Machida, Y., van Deursen, J.M., and Machida, Y.J. (2014). Spartan deficiency causes genomic instability and progeroid phenotypes. *Nat Commun* 5, 5744.

Moreno, S.P., Bailey, R., Champion, N., Herron, S., and Gambus, A. (2014). Polyubiquitylation drives replisome disassembly at the termination of DNA replication. *Science* 346, 477-481.

Morocz, M., Zsigmond, E., Toth, R., Enyedi, M.Z., Pinter, L., and Haracska, L. (2017). DNA-dependent protease activity of human Spartan facilitates replication of DNA-protein crosslink-containing DNA. *Nucleic Acids Res* 45, 3172-3188.

Nakano, T., Miyamoto-Matsubara, M., Shoulkamy, M.I., Salem, A.M., Pack, S.P., Ishimi, Y., and Ide, H. (2013). Translocation and stability of replicative DNA helicases upon encountering DNA-protein cross-links. *J Biol Chem* 288, 4649-4658.

O'Donnell, M.E., and Li, H. (2018). The ring-shaped hexameric helicases that function at DNA replication forks. *Nat Struct Mol Biol* 25, 122-130.

Reinisch, K.M., Chen, L., Verdine, G.L., and Lipscomb, W.N. (1995). The crystal structure of HaeIII methyltransferase covalently complexed to DNA: an extrahelical cytosine and rearranged base pairing. *Cell* 82, 143-153.

Rosado, I.V., Langevin, F., Crossan, G.P., Takata, M., and Patel, K.J. (2011). Formaldehyde catabolism is essential in cells deficient for the Fanconi anemia DNA-repair pathway. *Nat Struct Mol Biol* 18, 1432-1434.

Samel, S.A., Fernandez-Cid, A., Sun, J., Riera, A., Tognetti, S., Herrera, M.C., Li, H., and Speck, C. (2014). A unique DNA entry gate serves for regulated loading of the eukaryotic replicative helicase MCM2-7 onto DNA. *Genes & development* 28, 1653-1666.

Semlow, D.R., Zhang, J., Budzowska, M., Drohat, A.C., and Walter, J.C. (2016). Replication-Dependent Unhooking of DNA Interstrand Cross-Links by the NEIL3 Glycosylase. *Cell* 167, 498-511.

Stano, N.M., Jeong, Y.J., Donmez, I., Tummalapalli, P., Levin, M.K., and Patel, S.S. (2005). DNA synthesis provides the driving force to accelerate DNA unwinding by a helicase. *Nature* 435, 370-373.

Stingele, J., Bellelli, R., Alte, F., Hewitt, G., Sarek, G., Maslen, S.L., Tsutakawa, S.E., Borg, A., Kjaer, S., Tainer, J.A., *et al.* (2016). Mechanism and Regulation of DNA-Protein Crosslink Repair by the DNA-Dependent Metalloprotease SPRTN. *Mol Cell* 64, 688-703.

Stingele, J., Bellelli, R., and Boulton, S.J. (2017). Mechanisms of DNA-protein crosslink repair. *Nat Rev Mol Cell Biol* 18, 563-573.

Stingele, J., Schwarz, M.S., Bloemeke, N., Wolf, P.G., and Jentsch, S. (2014). A DNA-dependent protease involved in DNA-protein crosslink repair. *Cell* 158, 327-338.

Tanner, N.A., Loparo, J.J., and van Oijen, A.M. (2009). Visualizing Single-molecule DNA Replication with Fluorescence Microscopy. *J Vis Exp*.

Taylor, M.R.G., and Yeeles, J.T.P. (2018). The Initial Response of a Eukaryotic Replisome to DNA Damage. *Mol Cell* 70, 1067-1080 e1012.

Trowitzsch, S., Bieniossek, C., Nie, Y., Garzoni, F., and Berger, I. (2010). New baculovirus expression tools for recombinant protein complex production. *J Struct Biol* 172, 45-54.

Vannier, J.B., Sandhu, S., Petalcorin, M.I., Wu, X., Nabi, Z., Ding, H., and Boulton, S.J. (2013). RTEL1 is a replisome-associated helicase that promotes telomere and genome-wide replication. *Science* 342, 239-242.

- Vannier, J.B., Sarek, G., and Boulton, S.J. (2014). RTEL1: functions of a disease-associated helicase. *Trends Cell Biol* 24, 416-425.
- Vaz, B., Popovic, M., Newman, J.A., Fielden, J., Aitkenhead, H., Halder, S., Singh, A.N., Vendrell, I., Fischer, R., Torrecilla, I., *et al.* (2016). Metalloprotease SPRTN/DVC1 Orchestrates Replication-Coupled DNA-Protein Crosslink Repair. *Mol Cell* 64, 704-719.
- Vaz, B., Popovic, M., and Ramadan, K. (2017). DNA-Protein Crosslink Proteolysis Repair. *Trends Biochem Sci* 42, 483-495.
- Walter, J., and Newport, J. (2000). Initiation of eukaryotic DNA replication: origin unwinding and sequential chromatin association of Cdc45, RPA, and DNA polymerase alpha. *Mol Cell* 5, 617-627.
- Walter, J., and Newport, J.W. (1997). Regulation of replicon size in *Xenopus* egg extracts. *Science* 275, 993-995.
- Yardimci, H., Loveland, A.B., Habuchi, S., van Oijen, A.M., and Walter, J.C. (2010). Uncoupling of sister replisomes during eukaryotic DNA replication. *Molecular cell* 40, 834-840.
- Yardimci, H., Loveland, A.B., van Oijen, A.M., and Walter, J.C. (2012a). Single-molecule analysis of DNA replication in *Xenopus* egg extracts. *Methods*.
- Yardimci, H., Wang, X., Loveland, A.B., Tappin, I., Rudner, D.Z., Hurwitz, J., van Oijen, A.M., and Walter, J.C. (2012b). Bypass of a protein barrier by a replicative DNA helicase. *Nature* 492, 205-209.
- Yuan, Z., Bai, L., Sun, J., Georgescu, R., Liu, J., O'Donnell, M.E., and Li, H. (2016). Structure of the eukaryotic replicative CMG helicase suggests a pumpjack motion for translocation. *Nat Struct Mol Biol* 23, 217-224.

## Figure Legends

### Figure 1. Disappearance of the CMG footprint at DPC<sup>Lead</sup> is unaffected by proteolysis or p97 inhibition.

(A) Previous model of replication-coupled DPC repair (Duxin *et al.* 2014). (B) Schematic of what happens in the presence of Ub-VS (Duxin *et al.* 2014). (C) Grey inset: Schematic of nascent leading strand products released by AatII and FspI digestion of pmeDPC<sup>Lead</sup> or pDPC<sup>Lead</sup>. pDPC<sup>Lead</sup> or pmeDPC<sup>Lead</sup> were prebound with LacR to prevent one replication fork from colliding with the DPC. The plasmids were replicated in mock-depleted or SPRTN-depleted egg extract containing <sup>32</sup>P[α]-dATP and supplemented with buffer or p97 inhibitor (p97i). At different times, DNA was recovered and digested with AatII and FspI, separated on a denaturing polyacrylamide gel, and visualized by autoradiography. The lower autoradiogram shows nascent leading and lagging strands generated by the rightward replication fork, and the upper autoradiogram shows extension products. The CMG footprint is bracketed in blue (-30 to -37), and the products stalled at the adducted base are bracketed in orange (-1 to +1 and +12). The percentage of leading strands that underwent approach was quantified based on disappearance of the -30 CMG footprint (see methods), and the mean of five experiments is graphed. Error bars represent the standard deviation. Notably, stabilization of the DPC led to the appearance of stalling products from +1 to +12 (lanes 6-12) that were eliminated by REV1 depletion (Figure S1E). However, these products were absent with a normal DPC replicated in SPRTN-depleted extracts containing MG262 (data not shown), suggesting they are specific to DPC methylation. (D) pmeDPC<sup>2xLead</sup> was replicated in SPRTN-depleted egg extract supplemented with buffer or p97i (NMS-873). At different times, plasmid-associated proteins were recovered and blotted with the indicated antibodies. Samples were also withdrawn and examined for DPC proteolysis (Figure S1D).

**Figure 2. ssDNA downstream of an intact DPC facilitates CMG bypass.**

The indicated plasmids were prebound with LacR, replicated in SPRTN-depleted egg extracts, and analyzed as in Figure S1J. Disappearance of the CMG footprint (approach) was used as a proxy for CMG bypass and quantified as in Figure 1C (see methods). The mean of three experiments is shown. Error bars represent the standard deviation.

**Figure 3. RTEL1 is required for efficient CMG bypass.**

**(A)** Recovery of 5' to 3' helicases in the mass spectrometry dataset of Larsen et al. (*submitted*).

The heat map shows the relative abundance of the indicated proteins (expressed as a z-score with yellow indicating higher abundance) in the indicated conditions. To identify proteins whose binding is replication-dependent, pCTRL and pDPC were incubated in extracts containing geminin, a replication licensing inhibitor. **(B)** Mock-depleted, RTEL1-depleted, and RTEL1-depleted egg extracts supplemented with wild-type RTEL1 or RTEL1-K48R were blotted with RTEL1 and ORC2 (loading control) antibodies. **(C)** Egg extracts were depleted of SPRTN and either mock or RTEL1 depleted, as indicated, and supplemented with buffer, wild-type RTEL1, or RTEL1-K48R. Leading strand approach was visualized as in Figure S1J and quantified as in Figure 1C. The mean of three experiments is shown. Error bars represent the standard deviation. **(D)** pmeDPC<sup>Lead</sup> or pmeDPC<sup>Lag</sup> was replicated in the indicated extracts and analyzed as in Figure 1C. CMG bypass was quantified as in Figure 1C. **(E)** Egg extracts were depleted of SPRTN and either mock or RTEL1 depleted, and supplemented with buffer or IPTG (at 5 minutes after replication initiation) and Buffer or p97 inhibitor (p97i), as indicated. Leading strand approach was visualized as in Figure S1J and quantified as in Figure 1C. The mean of three experiments is shown. Error bars represent the standard deviation. To measure fork convergence, DNA samples from (E) were digested with the single cutter AflIII, resolved by native agarose gel electrophoresis, and visualized by autoradiography (Figure S3F). The

slower CMG bypass observed in RTEL1-depleted extract containing IPTG relative to mock-depleted extract (light blue vs. red graph) is largely accounted for by the fact that CMG progression through lacO array is delayed by LacR, even in the presence of IPTG, as seen from the slower appearance of resolved, linear species in Figure S3F (compare light blue vs. red graphs).

**Figure 4. RTEL1 is required for efficient DPC proteolysis.**

(A) pDPC<sup>2xLead</sup> was replicated in mock-depleted or RTEL1-depleted egg extract and supplemented with buffer, wild-type RTEL1, or RTEL1-K48R. At the indicated times, plasmid was recovered under stringent conditions, the DNA digested, and the resulting samples blotted for HpaII. Signal from the entire lane was quantified, and peak signal was assigned a value of 100%. The mean of three independent experiments is shown. Error bars represent standard deviation. (B) Parallel reactions to those in (A) were supplemented with [ $\alpha$ -<sup>32</sup>P]dATP. Leading strand approach was visualized as in Figure S1J and quantified as in Figure 1C. (C) pmeDPC<sup>2xLead</sup> was replicated in the indicated extracts. Samples were withdrawn and processed by the stringent pull-down procedure described in Figure 4A. Short and long (lower panel) exposures of the same blot are shown. (D) pmeDPC<sup>2xLead</sup> or pmeDPC<sup>2xLead</sup> Lead were replicated in non-depleted extract. Stringent plasmid pull downs were performed as in Figure 4A and presented as in (C). (E) pDPC<sup>2xLead</sup> was replicated in mock-depleted or RTEL1-depleted egg extracts, and stringent plasmid pull-down was performed and analyzed as in Figure 4A. Functional RTEL1 depletion was verified in Figure S4B. (F) pDPC<sup>2xLead</sup> was replicated in the indicated egg extracts that also contained DMSO or MG262. Stringent plasmid pull-down was performed as in Figure 4A.

### Figure 5. KEHRMIT – a single molecule assay for CMG dynamics

(A) KEHRMIT assay (see Main text and methods for details). (B) Coomassie-stained SDS-PAGE gel of purified recombinant GINS before and after sortase labeling of Psf3 with AF647, which shifts its mobility (arrow). (C) Kymogram of a replication bubble from a KEHRMIT experiment. GINS<sup>AF647</sup> signal is shown in green. The blue signal corresponds to Fen1<sup>mKikGR</sup> - a fluorescent protein that binds nascent DNA (Loveland et al., 2012). (D-E) Beeswarm plot of CMG speed and processivity (i.e. distance travelled) measured via KEHRMIT (dots represent individual helicase molecules). Blue line, mean; gray box, 95% Confidence Interval (CI) estimated by bootstrapping.

### Figure 6. Direct observation of DPC bypass by CMG

(A) Image of a stretched and immobilized DNA-DPC substrate. DNA is stained with sytox orange (top panel). The DPC is labeled on its C-terminus with AF568 (middle panel). (B) Cartoons depicting how the location of initiation determines whether CMGs encounter DPC<sup>Lead</sup> (top) or DPC<sup>Lag</sup> followed by DPC<sup>Lead</sup> (bottom) (C) Kymogram of a meDPC substrate undergoing replication in SPRTN-depleted extract from an origin that fired between the two lesions. Both CMGs undergo DPC bypass. Images were acquired at 1 min/frame. Green, AF647; pink, AF568. (D) Quantification of five different classes of CMG-DPC<sup>Lead</sup> encounters in two biological repeats: (i) Bypass of intact DPC (BID), representing unambiguous bypass events; (ii) DPC disappeared first, followed by CMG departure from the pause site (DD+). When proteolysis was inhibited (meDPC, ΔSPRTN extract), DD+ events likely involve DPC bypass but do not meet the BID criteria due to DPC photobleaching; (iii) DPC disappeared first, without CMG departure from the pause site (DD-), including potential bypass events where CMG photobleached or DNA ruptured soon after the DPC signal vanished; (iv) CMG

disappeared first (CD), likely due to photobleaching, obscuring any subsequent bypass events; (v) CMG and DPC disappeared together (DT), including events where the experiment ended or the DNA ruptured before bypass could be detected. Due to rounding errors, the total probability does not always add up to exactly 100%. (E) Beeswarm plot of the time needed to bypass meDPC<sup>Lead</sup> or meDPC<sup>Lag</sup> in SPRTN-depleted extract. Blue lines and gray boxes correspond to the mean and the 95% CI for the mean, respectively. (F) Same as (C) but showing a kymogram in which an origin fired to the right of both lesions. The leftward-moving helicase (green) first bypassed a meDPC<sup>Lag</sup> in ~1 min, then reached a meDPC<sup>Lead</sup> where it paused. (G) Beeswarm plot of DPC lifetime after CMG arrival at the lesion. Blue lines and gray boxes as in (E). (H) Beeswarm plot of CMG speed during approach to and departure from DPC lesions versus the speed of aphidicolin-uncoupled helicases. Blue lines and gray boxes as in (E). The aphidicolin condition was performed on  $\lambda$  DNA. (I) Kymogram of CMG-meDPC<sup>Lead</sup> encounter (SPRTN-depleted extract) that resulted in DPC bypass and CMG uncoupling, followed by apparent re-coupling (white arrow).

**Figure 7. RTEL1 is required for CMG bypass of non-covalent nucleoprotein complexes.**

(A) Top, structures generated with and without XmnI digestion before and after forks pass through the LacR array. (B) pLacO<sub>32</sub> was pre-incubated with LacR and replicated in the indicated egg extracts containing [ $\alpha$ -<sup>32</sup>P]dATP. At different times, DNA was recovered, digested with the single cutter XmnI, resolved by native agarose gel electrophoresis, and visualized by autoradiography. (C) DNA samples from (B) were nicked with Nt. BspQI to release the rightward leading strand (red arrow), separated on a denaturing polyacrylamide gel, and visualized by autoradiography. *lacO* sites are located ~30 nt downstream of each stalling product (Dewar et al., 2015). (D) Model for RTEL1 bypass of nucleoprotein complexes, and possible mechanisms of DPC bypass by CMG. When the replisome encounters a

nucleoprotein barrier, CMG stalls and RTEL1, which appears to travel with the fork, becomes engaged. In the case of non-covalent nucleoprotein complexes, RTEL1 and CMG cooperate to unwind the DNA underlying the protein, leading to its displacement and immediate resumption of fork progression. At a covalent DPC, RTEL1 translocates along the undamaged lagging strand template, exposing ssDNA at the DPC and beyond. The generation of ssDNA facilitates CMG bypass of the DPC. Given the high affinity of pol  $\epsilon$  (grey oval) for CMG, we envision that it bypasses the DPC with CMG. Once CMG has bypassed the DPC, the DPC undergoes proteolysis by SPRTN or the proteasome (see Larsen et al., *submitted*). Finally, the leading strand is extended past the peptide adduct using translesion synthesis polymerases.

## Methods

All ensemble experiments were performed three or more times, except for Figure 3D which was performed twice. All single-molecules experiments were performed two or more times.

### Preparation of DNA Constructs

To generate pDPC, we first created pJLS2 by replacing the AatII-BsmBI fragment from pJD2 (Duxin et al., 2014) with the a sequence (5'-

GGGAGCTGAATGCCGCGCGAATAATGGTTTCTTAGACGT-3') which contains a Nb.BsmI site. To generate pDPC<sup>2xLead</sup> the SacI-BssHII fragment from pJLS2 was replaced with the following sequence: 5'-

CATCCACTAGCCAATTTATGCTGAGGTACCGGATTGAGTAGCTACCGGATGCTGAGGGG ATCCACTAGCCAATTTATCATGG-3'. To generate pDPC<sup>ICL</sup>, we first created pJLS6 by

replacing the SacI-BssHII fragment of pJLS2 with a sequence (5'-

CGAAGACAACCCTTAAACAGCTGAAAGAAGACGCGTGCG-3') that contains two BbsI sites.

The cisplatin ICL containing oligonucleotides were inserted as previously described (Enoiu et al., 2012). To generate pDPC<sup>Lag/Lead</sup>, and pDPC<sup>Lag/Lead-Bubble</sup> we first replaced the BssHII-KpnI fragment from pJLS2 with the sequence 5'-

CGCGCTTAATCAGTGAGGCACCTATCTCCGGTCTGAGTCATGCGTAACTCGAGTGCTTGT AGTGGATTTACCGGATTGAGTAGCTACCGGATGGTAC-3' hybridized with either 5'-

CATCCGGTAGCTACTCAATCCGGTAAATCCACTACAAGCACTCGAGTTACGCATGACTCA GACCGGAGATAGGTGCCTCACTGATTAAG-3' or

CATCCGGTAGCTACTCAATCCGGTATTAGGTGATGTTTCGTGAGCTCAATGCGTACTGAGT CTGGCGAGATAGGTGCCTCACTGATTAAG -3', respectively. The supercoiled band was

purified by cesium chloride gradient ultracentrifugation and DNA was subsequently crosslinked to methylated M.HpaII-His<sub>6</sub>, as previously described (Duxin et al., 2014). pJLS2, pJLS6<sup>ICL</sup>, or

pJLS3 were nicked with Nt.Bbvcl and ligated with an oligonucleotide containing a fluorinated cytosine (5'-TCAGCATCCGGTAGCTACTCAATC[C5-Fluor dC]GGTACC-3') and subsequently crosslinked to M.HpaII-His<sub>6</sub> or methylated M.HpaII-His<sub>6</sub> to generate pDPC<sup>Lead</sup>, pDPC<sup>ICL</sup>, pDPC<sup>2xLead</sup> or pmeDPC<sup>Lead</sup>, pmeDPC<sup>ICL</sup>, and pmeDPC<sup>2xLead</sup>, respectively, as previously described (Duxin et al., 2014). To create pmeDPC<sup>Lead/Lag</sup>, pJLS2 was first nicked with Nt.Bbvcl and ligated with an oligonucleotide containing a fluorinated cytosine (5'-TCAGCATC[C5-Fluor dC]GGTAGCTACTCAATCCGGTACC-3'). It was subsequently nicked with Nb.Bbvcl and ligated with a second oligonucleotide containing a fluorinated cytosine (5'- TGAGGTAC[C5-Fluor dC]GGATTGAGTAGCTACCGGATGC-3') before crosslinking to methylated M.HpaII-His<sub>6</sub>. To create pmeDPC<sup>Lag/Lead</sup> pJLS2 was first nicked with Nt.Bbvcl and ligated with an oligonucleotide containing a fluorinated cytosine (5'-TCAGCATCCGGTAGCTACTCAATC[C5-Fluor dC]GGTACC-3'). It was subsequently nicked with Nb.Bbvcl and ligated with a second oligonucleotide containing a fluorinated cytosine (5'- TGAGGTACCGGATTGAGTAGCTAC[C5-Fluor dC]GGATGC-3') before crosslinking to methylated M.HpaII-His<sub>6</sub>. To create pmeDPC<sup>Lead/Lead</sup> or pmeDPC<sup>2xLeadLead</sup>, pJLS2 or pJLS3 was nicked with Nt.Bbvcl and ligated with an oligonucleotide containing two fluorinated cytosines (5'-TCAGCATC[C5-Fluor dC]GGTAGCTACTCAATC[C5-Fluor dC]GGTACC-3') and subsequently crosslinked to methylated M.HpaII-His<sub>6</sub> to generate pmeDPC<sup>Lead/Lead</sup> or pDPC<sup>2xLeadLead</sup>, respectively, as previously described (Duxin et al., 2014). Creation of pDPC<sup>ssDNA</sup> and pmeDPC<sup>ssDNA</sup> is described in (Larsen et al. *submitted*). Creation of pLacO<sub>32</sub> was previously described (Dewar et al., 2015).

### ***Xenopus* Egg Extracts and DNA Replication**

*Xenopus* egg extracts were prepared and utilized essentially as described (Lebofsky et al., 2009). Briefly, licensing was carried out by supplementing a high-speed supernatant (HSS) of

egg cytoplasm with plasmid DNA at a final concentration of 7.5–15 ng/μL. For radiolabeling DNA replication products, [ $\alpha$ - $^{32}$ P] dATP was added to HSS prior to the DNA. For replication in the presence of Lacl, 1 volume of plasmid (75 ng/μL) was incubated with an equal volume of 12 μM Lacl for 30 minutes prior to transfer into HSS so that the final concentration of plasmid was 7.5 ng/μL (Duxin et al.). Licensing mixes were incubated for 30 min at room temperature to assemble pre-replicative complexes (pre-RCs). To prevent licensing, Geminin was added to HSS at a final concentration of 10 μM and incubated for 10 min at room temperature prior to addition of plasmid DNA. To initiate replication, 1 volume of licensing reaction was mixed with 2 volumes of nucleoplasmic extract (NPE) that had been diluted two-fold with 1xELB-sucrose (10 mM Hepes-KOH pH 7.7, 2.5 mM MgCl<sub>2</sub>, 50 mM KCl, 250 mM sucrose). 0.5 μl aliquots of replication reaction were typically stopped with 5–10 volumes of replication stop buffer (8 mM EDTA, 0.13% phosphoric acid, 10% ficoll, 5% SDS, 0.2% bromophenol blue, 80 mM Tris-HCl at pH 8), treated with 1 μg/μL Proteinase K. For nascent strand analysis, 2.5 μl aliquots of replication reaction were stopped in 10 volumes of sequencing stop buffer (0.5 % SDS, 25 mM EDTA, 50 mM Tris-HCl pH 8.0) followed by addition of 1.25 μl of 190 ng/μL RNase A and incubated for 30 minutes at 37 °C. After RNase digestion, 1.25 μl of 900 ng/μL Proteinase K was added to the DNA samples and incubated overnight at room temperature. Following the Proteinase K treatment, samples were diluted to 150 μl with 10 mM Tris-HCl pH 8.0. The samples were extracted once with an equal volume of phenol/chloroform followed by one extraction with an equal volume of chloroform. The DNA was then precipitated with the addition of 0.1 volumes 3M sodium acetate pH 5.2 and 1 μl glycogen (20 mg/ml stock) and resuspended in 7.5 μl. For RTEL1 immunodepletion and rescue experiments, NPE was supplemented with ~ 200 nM recombinant wild type or mutant *Xenopus* RTEL1 and incubated for 15 minutes prior to replication initiation. For p97i (NMS873; Sigma Cat# SML1128) treatment, NPE was supplemented with 200 μM NMS-873 (20 mM stock) and incubated for 10

minutes prior to mixing with HSS (133.33  $\mu\text{M}$  final concentration in replication mix. For MG262 (stock 20 mM; Boston Biochem.Cat# I-120) treatment, NPE was supplemented with 200  $\mu\text{M}$  MG262 and incubated for 15 minutes prior to mixing with HSS (133.33  $\mu\text{M}$  final concentration in replication mix). A 1 mM Cdc7-i (PHA-767491; Sigma Cat# PZ0178) stock was prepared in ELB-sucrose buffer and added to replication mix at a final working concentration of 100  $\mu\text{M}$  at the specified time point. For ATRi (ETP-46464; Sigma Cat# SML1321) treatment, NPE was supplemented with 100  $\mu\text{M}$  ATRi and incubated for 10 minutes prior to mixing with HSS (66.67  $\mu\text{M}$  final concentration in replication mix). For aphidicolin (Sigma Cat# A0781) treatment, replication mix was supplemented with 150  $\mu\text{M}$  aphidicolin. For IPTG (stock 1 M; Sigma Cat# I5502) treatment, replication reactions were supplemented with 300  $\mu\text{M}$  IPTG 5 minutes after replication initiation. Samples were analyzed by native 0.8% agarose gel electrophoresis. Gels were exposed to phosphorscreens and imaged on a Typhoon FLA 7000 phosphorimager (GE Healthcare). To better visualize products in Figure 3D (bottom panel), the original images were converted into a log scale for display by applying the function  $f(p) = \log(p) * 255 / \log(255)$  to each pixel ( $p$ ) in the images. Band or total lane intensities were quantified using Multi-Gauge software (Fujifilm) with subtraction of appropriate background.

### **Nascent strand analysis**

To nick radio-labeled nascent leading-strands, 3-4  $\mu\text{l}$  of extracted and ethanol precipitated DNA (see above) at 1-2  $\text{ng } \mu\text{l}^{-1}$  was incubated in 1x buffer 3.1 (New England BioLabs) with 0.45 units  $\mu\text{l}^{-1}$  Nb.Bsml (New England BioLabs) in a 5  $\mu\text{l}$  reaction at 65  $^{\circ}\text{C}$  for 1 h. To digest radio-labeled nascent leading-strand 3-4  $\mu\text{l}$  of extracted and ethanol precipitated DNA a 1-2  $\text{ng } \mu\text{l}^{-1}$  was incubated in 1x cutsmart buffer (New England BioLabs) with 1 unit  $\mu\text{l}^{-1}$  AatII (New England BioLabs) and FspI (New England BioLabs) in a 5  $\mu\text{l}$  reaction at 37  $^{\circ}\text{C}$  for 2 h. To nick rightward leading strands of pLacO<sub>32</sub>, 3-4  $\mu\text{l}$  of purified DNA at 1-2  $\text{ng } \mu\text{l}^{-1}$  was incubated in

buffer 3.1 with 0.4 units  $\mu\text{l}^{-1}$  Nt.BspQI (New England BioLabs) at 37 °C for 1 h. Digestion reactions were stopped with 0.5 volumes of Sequencing Stop solution (95% formamide, 20 mM EDTA, 0.05 % bromophenol blue, 0.05% xylene cyanol FF). Nicked DNA (3.5 to 4  $\mu\text{l}$  samples) was separated on 4 % (for pLacO) or 7% (pDPC) polyacrylamide sequencing gels. Gels were dried and subjected to phosphorimaging using a Typhoon FLA 7000 phosphorimager. Gels were quantified using Multi Gauge software (Fuji Photo Film Co.). For Figure 6A, 1  $\mu\text{l}$  of purified DNA was used for XmnI digestion.

After leading strands stall at the -30 to -44 positions, they approach to the -1 to +1 positions relative to the DPC. Intermediates between these two clusters are also observed, but not when the DPC cannot be ubiquitylated (e.g. Figure 1C; (Duxin et al., 2014)). The question arose whether these intermediates are associated with CMGs that have bypassed or not. Importantly, our single molecule data demonstrates that CMG bypasses a DPC with similar kinetics whether or not the DPC is ubiquitylated (Figure S6J). These results indicate that these approach intermediates are generated after CMG bypass, probably due to polymerase stalling at ubiquitylated DPCs. Therefore, to quantify the percentage of CMG that underwent bypass in Figures 1C, 2, 3C, 3E, 4B, S3D, and S3E (called “approach” in Figure 1C, where bypass had not yet been established), the radioactive signal of all leading strands located between positions +1 and -29 on the gel (reflecting CMGs that have bypassed) was divided by the radioactive signal for leading strands between positions +1 and -44 (reflecting CMGs that have stalled at the lesion or undergone bypass). In the case of pmeDPC<sup>Lead/Lead</sup> (Figure 2, lanes 13-18), we divided the signal between +1 of the 2<sup>nd</sup> DPC and -1 of the 1<sup>st</sup> DPC (both DPCs bypassed) by the signal between +1 of the 2<sup>nd</sup> DPC and -44 of the first DPC (bypassed and not bypassed).

## **Antibodies and Immunodepletion**

The xIRTEL1-N antibody was raised against a fragment of *Xenopus laevis* RTEL1 encompassing amino acids 400-654, which was tagged on its N-terminus with His<sub>6</sub>. The protein fragment was overexpressed and purified from bacteria under denaturing conditions, and the antibody was raised by Pocono Rabbit Farm & Laboratory. The RTEL1 antibody was affinity purified from the serum using the RTEL1 antigen according to standard protocols. The xIRTEL1-C antibody was raised against amino acids 428-443 (Ac-HPDTSQRKKPRGDIWSC-amide) by New England Peptide. The FancM antibody was raised against a FancM peptide by Bethyl Laboratories. The following antibodies were described previously: CDT1 (Arias and Walter, 2005), Orc2 (Walter and Newport, 1997), CDC45 (Walter and Newport, 2000), M.Hpall (Larsen, et al., *submitted*), PSMA3 (Larsen, et al., *submitted*), SPRTN-N (Larsen, et al., *submitted*), Chk1-p(Ser345) (Cell Signaling Cat #2341L), and Histone H3 (Cell Signaling Cat #9715S). Mcm6 antibody was raised against a C-terminal peptide (Ac-CLVVNPNYMLED-OH) and affinity purified. The most prominent band it recognized in Western blotting of total extract was 115 kD, and it recognized the same band in protein preparations containing recombinant MCM6. Two rabbits (#34299 and #34300) were immunized with purified GINS (Pocono Rabbit Farm and Laboratory). Anti-GINS antibodies were affinity-purified from serum using GINS immobilized on AminoLink Coupling Resin (Thermo Fisher Cat# 20381). 2-4mg of purified GINS was cross-linked to 1mL of resin according to the manufacturer's protocol. Purified antibody was dialyzed into 1x TBS buffer, concentrated to 1mg/mL final concentration, and stored at -80C.

For RTEL1 immunodepletion, 3.5 volumes of purified RTEL1 antibody (1 mg mL<sup>-1</sup>) or an equivalent amount of rabbit IgG purified from non-immunized rabbit serum (Sigma) were incubated with 1 volume of Protein A Sepharose Fast Flow (PAS) (GE Healthcare) overnight at 4°C. For FancM immunodepletion, 4 volumes of FancM (1 mg mL<sup>-1</sup>) or an equivalent amount of rabbit IgG purified from non-immunized rabbit serum (Sigma) were incubated with 1 volume

of Protein A Sepharose Fast Flow (PAS) (GE Healthcare) overnight at 4°C. For SPRTN immunodepletion, 4 volumes of SPRTN serum was incubated with 1 volume of Protein A Sepharose Fast Flow (PAS) (GE Healthcare) overnight at 4°C. For mock depletion, 4 volumes of preimmune serum from matched rabbit, was used. One volume of antibody-conjugated Sepharose was then added to 5 volumes of precleared HSS or NPE and incubated for 1 hour at 4°C. The HSS or NPE was collected and incubated two more times with antibody-conjugated sepharose for a total of three rounds of depletion. The depleted HSS or NPE was collected and used immediately for DNA replication, as described above.

### **Protein Expression and Purification**

M.Hpall-His<sub>6</sub>, LacI-biotin, and LacI-His<sub>6</sub> were expressed and purified as previously described (Duxin et al. 2014). Lysine methylation of M.Hpall was carried out as described (Larsen, et al., *submitted*). *Xenopus* RTEL1 open reading frame with an N-terminal GST tag separated by a 3C cleavage site was cloned into pFastBac1 (Thermo Fisher Scientific) using custom gene synthesis from Integrated DNA Technologies (IDT). The RTEL1 sequence was confirmed by Sanger sequencing. Mutants of RTEL1 were created by around-the-horn site-directed mutagenesis, and mutations were confirmed by Sanger sequencing. The GST-RTEL1 Baculoviruses were made using the Bac-to-Bac system (Thermo Fisher Scientific) according to the manufacturer's protocols. GST-RTEL1 and mutants were expressed in 3 L suspension cultures of Sf9 cells (Thermo Fisher Scientific) by infection with RTEL1 baculovirus for 36-48 hrs. Sf9 cells were collected via centrifugation and washed with 1XPBS and subsequently pelleted by centrifugation and flash frozen. Cell pellets were thawed and resuspended in an equal volume of 2X Lysis Buffer (100 nM HEPES pH7.5, 1 M NaO<sub>2</sub>Ac, 20 % sucrose, 0.2 % IGEPAL, 4 mM DTT, 2X Roche EDTA-free Complete protease inhibitor cocktail), 1X Lysis Buffer (50 mM HEPES pH7.5, 500 mM NaO<sub>2</sub>Ac, 10 % sucrose, 0.1 % IGEPAL, 2 mM DTT, 1X

Roche EDTA-free Complete protease inhibitor cocktail) to the weight of the cell pellet. Cells were lysed by two rounds of sonication, followed by addition of ammonium sulfate (4M stock) to 200 mM final concentration and 45  $\mu$ l/ml Polymin P (10 % stock) and stirred at 4 °C for 10 minutes. Lysate was cleared by ultracentrifugation at 25,000 rpm in a Beckman Ti45 rotor for 1 hour. The supernatant was subjected to ammonium sulfate precipitation using 0.2 g/ml ammonium sulfate. Proteins were pelleted by ultracentrifugation at 25,000 rpm in a Beckman Ti45 rotor for 1 hour. The supernatant was discarded and protein pellets were resuspended in 50 ml Wash Buffer A<sub>500</sub> (25 mM HEPES pH7.5, 500 mM NaO<sub>2</sub>Ac, 10 % sucrose, 0.01 % IGEPAL, 2 mM DTT, 1X Roche EDTA-free Complete protease inhibitor cocktails). The resuspended pellet was incubated for 2 hours with 300  $\mu$ l of Glutathione sepharose™ 4B (GE) at 4 °C. Following incubation, resin was first washed with 20 ml of Wash Buffer A<sub>500</sub> and then with 10 ml of Wash Buffer A<sub>200</sub> (25 mM HEPES pH7.5, 200 mM NaO<sub>2</sub>Ac, 10 % sucrose, 0.01 % IGEPAL, 2 mM DTT, 1X Roche EDTA-free Complete protease inhibitor cocktails). Proteins were eluted from the resin with Elution Buffer E<sub>200</sub> (25 mM HEPES pH7.5, 200 mM NaO<sub>2</sub>Ac, 10 % sucrose, 0.005 % IGEPAL, 2 mM DTT, 20 mM L-glutathione reduced, pH adjusted to 8.0). Fractions were pooled and dialyzed against Dialysis Buffer (25 mM HEPES pH7.5, 200 mM NaO<sub>2</sub>Ac, 10 % sucrose, 0.005 % IGEPAL, 2 mM DTT) with addition of HRV 3C protease (Thermo Fisher) at 4°C for 4 hr. Aliquots of RTEL1 were flash frozen and stored at -80°C.

### **Plasmid Pull-Down**

The plasmid pull-down assay was performed as described (Budzowska et al., 2015). Briefly, streptavidin-coupled magnetic beads (Invitrogen; 10  $\mu$ l per pull-down) were washed three times with 50 mM Tris (pH 7.5), 150 mM NaCl, 1 mM EDTA pH 8, 0.02% Tween-20. Biotinylated LacI was added to the beads (4 pmol per 10  $\mu$ l beads) and incubated at room

temperature for 40 min. The beads were then washed four times with Pull-down Buffer (10 mM HEPES (pH 7.7), 50 mM KCl, 2.5 mM MgCl<sub>2</sub>, 250 mM sucrose, 0.25 mg/ml BSA, 0.02% Tween-20) and resuspended in 40 µl of the same buffer. The bead suspension was stored on ice until needed. At the indicated times, 4.0 µl samples of the replication reaction were withdrawn and gently mixed with Lacl-coated streptavidin Dynabeads. The suspension was immediately placed on a rotating wheel and incubated for 30 min at 4 °C. The beads and associated proteins were isolated by centrifugation through a sucrose cushion (10 mM HEPES pH 7.7, 2.5 mM MgCl<sub>2</sub>, 50 mM KCl, 0.5 M sucrose, 0.02 % Tween), then washed once with Pull-down Buffer. All residual buffer was removed, and the beads were resuspended in 20 µl of 2X Laemmli sample buffer. Equal volumes of the protein samples were blotted with the indicated antibodies.

### **DPC pull-down**

The DPC pull-down assay to quantify how much M.HpaII was removed from the plasmid during DPC repair was performed as described (Larsen et al., *submitted*).

### **KEHRMIT**

#### **Cloning, Expressing, and Purifying Recombinant GINS**

Codon-optimized *Xenopus laevis* cDNAs encoding all four GINS subunits (synthesized by IDT) were cloned into a single expression plasmid (pGC128) using the MultiBac system (Trowitzsch et al., 2010). A sequence encoding a 10-aa linker, the LPETG tag for sortase labeling, and a His6 tag was added to the C-terminus of the Psf3 subunit (GGGGSGGGGS-LPETG-HHHHHH). The bacmid encoding the GINS complex was obtained by electroporating pGC128 into DH10EMBacY (or DH10Bac) electro-competent cells and purified using ZR BAC DNA miniprep kit (Zymo Research Cat# D4048).

Baculovirus encoding GINS was amplified in three stages (P1, P2, and P3) in Sf9 cells (Expression Systems Cat# 94-001S) and GINS expression levels were monitored via western blots. 500mL of Tni cell culture (Expression Systems Cat# 94-002S) at a density of 2-3 was infected with 5-10 mL P3 baculovirus (MOI>1). Cells harvested 48 hrs post-infection were pelleted at 500 x g for 15min and re-suspended in a final volume of 50mL in GINS Lysis Buffer (GLB) containing 20mM Tris-HCl pH8.0, 5% glycerol, 500mM NaCl, 20mM Imidazole, 1mM DTT, 1mM PMSF, EDTA-free cOmplete protease inhibitor cocktail (Roche Cat # 11873580001). Cells were lysed by sonication on ice and the insoluble fraction was pelleted via centrifugation for 1hr at 30,000g at 4C. The clarified lysate was incubated with 0.5mL NiNTA resin (QIAGEN Cat# 30410) for 1hr at 4C on a rotating wheel. The resin was washed 5 times with 10mL of GLB in a disposable column. The protein was eluted in 5 rounds with 500uL/each of GLB + 250 mM Imidazole; the elutions were pooled and desalted using a PD10 column (GE Healthcare Cat 17-0851-01) into 20mM Tris-HCl pH7.5, 5% glycerol, 100mM NaCl, 1mM DTT. Recombinant GINS was further purified on a MonoQ column connected to an AKTA Pure FPLC with a 100-1000mM NaCl gradient in 20mM Tris-HCl pH7.5, 5% glycerol, 1mM DTT buffer (the GINS complex eluted at ~500mM NaCl). The eluted protein was desalted using PD10 columns or dialysis into 20mM Tris-HCl pH7.5, 5% glycerol, 150mM NaCl, 1mM DTT; concentrated to ~2mg/mL, frozen in liquid nitrogen, and stored at -80C. A pellet from 0.5L of Tni cell culture yielded ~5mg of purified GINS.

### **Cloning and Purification of HpalI for Sortase Labeling**

A sequence encoding a 10-aa linker, the LPETG tag for sortase labeling, and a His6 tag was added to the C-terminus of HpalI (pGC220) and expressed in T7 Express cells (NEB Cat# C25661) (Duxin et al., 2014). LPETG-tagged HpalI was affinity purified on NiNTA resin, and further purified on a MonoQ column connected to an AKTA Pure FPLC with a 100-500mM KCl

gradient in 20mM HEPES pH8.2, 10% glycerol, 0.02% IGEPAL-630, 1mM DTT (Hpall eluted at ~300mM KCl). The fractions containing Hpall were pooled and dialyzed overnight into 20mM HEPES pH8.0, 100mM KCl, 10% glycerol, 0.02% IGEPAL-630, 1mM DTT; concentrated to ~2-3 mg/mL; and stored at -80C. A portion of LPETG-tagged Hpall was methylated as described above, then fluorescently labeled using sortase.

### **Fluorescent Labeling of GINS and Hpall**

Sortase-tagged proteins were conjugated to a short peptide labeled with a fluorophore (AF647 or AF568). 1mg of lyophilized GGGGYKCK peptide (synthesized by New England Peptide) was dissolved in 1mL degassed reaction buffer (20mM Hepes pH 7.5, 0.1mM EDTA, 10mM TCEP) and incubated at room temperature for 15 min. 1mg of AF647-maleimide (Thermo Fisher Cat# A20347) or 1mg of AF568-maleimide (Thermo Fisher Cat# 20341) was dissolved in 40 $\mu$ L degassed DMSO and added to the dissolved peptide, then incubated on a rotating wheel at room temperature for 3 hrs. The reaction was quenched with 10mM DTT. The labeled peptide was separated from unlabeled peptide and un-reacted fluorophore on a MonoQ column with a 10mM-1000mM ammonium carbonate pH 7.8-8.0 gradient (pH adjusted using 50% acetic acid). Fractions containing the labeled peptide were pooled and lyophilized, then dissolved in 50 $\mu$ L 20 mM HEPES pH7.5 and stored at -80C.

Conjugation reaction: 2 nanomoles of GINS or 5 nanomoles of Hpall or meHpall were reacted overnight at 4°C on a rotating wheel with 20x molar excess of GGGGYKCK<sup>AF647</sup> or GGGGYKCK<sup>AF568</sup> in the presence of 1/10x molar excess of sortase enzyme (purified as previously described (Chen et al., 2011)), supplemented with 100 $\mu$ L 4x sortase buffer, in a 400 $\mu$ L total volume. 4x Sortase Buffer consists of 80mM HEPES pH 7.5, 600mM NaCl, 40% glycerol, 4mM DTT, and 20mM CaCl<sub>2</sub>. After incubation, the reaction mixture was

supplemented with NaCl to a final concentration of 500mM and imidazole to a final concentration of 10mM, and incubated with 40 $\mu$ L NiNTA resin for 1hr at 4C. NiNTA trapped unlabeled protein and the His6-tagged sortase whereas labeled protein and excess free peptide remained in the supernatant. Labeled protein was purified and desalted by gel filtration on a Superdex200 column in 20mM Tris-HCl pH7.5, 150mM NaCl, 10% glycerol, and 1mM DTT; then concentrated to 1mg/mL and stored at -80C for up to 1 yr.

### **Preparing the Single-Molecule Substrate with Fluorescently Labeled DPC Lesions**

The DNA substrate was cloned and assembled by tandem recombineering using the MultiBac system (Trowitzsch et al., 2010) as a 30.6 kb plasmid (pGC261) and grown in DH10 $\beta$  cells (NEB Cat# C3019I). The plasmid contains two sites for HpaII conjugation flanked by Nt.BbvCI sites such that a fluorinated oligo can be annealed and ligated into the backbone. 100-150 $\mu$ g (at ~1000 ng/ $\mu$ L) of pGC261 plasmid was purified using a Midi Prep kit (QIAGEN) from 250mL of bacterial culture. Supercoiled plasmid was nicked with Nt.BbvCI (NEB Cat# R0632S) and the enzyme was heat inactivated. 20-fold molar excess of modified oligo (TCAGCATCCGGTAGCTACTCAATCCGGTACC, the highlighted nucleotide is 5-fluoro-deoxycytidine, synthesized by BioSynthesis) was annealed to the nicked backbone then ligated overnight. The DNA was dialyzed in 10mM TrisHCl pH8.0, then digested with the single cutter NotI-HF (NEB Cat# R3189S) in NEB2 buffer and the enzyme was heat-inactivated. The 3' DNA termini were biotinylated by incorporating biotin-dCTP (Thermo Fisher Cat# 19518018) and biotin-dGTP (Perkin Elmer Cat# NEL541001EA) using Klenow Fragment 3'→5' exo- (NEB Cat# M0212S). The DNA was then purified by electrophoresis on a 0.6% agarose 1xTAE gel pre-stained with SYBR Safe (Thermo Fisher Cat# S33102), the 30.6kb linear DNA band was excised and electro-eluted in 1xTAE Buffer. The DNA was butanol-extracted several times until the volume was reduced 2-3 fold, then phenol-chloroform extracted 3 times to remove any

agarose traces, followed by chloroform extraction. The DNA was ethanol-precipitated and eluted in EB (QIAGEN), and dialyzed in 10mM Tris-HCl H8.0 to remove trace contaminants. Purified DNA was conjugated to 100-fold molar excess of HpaII<sup>AF568</sup> or meHpaII<sup>AF568</sup> in 1x CutSmart buffer (NEB Cat# B7204S) supplemented with 0.1mM SAM (NEB Cat# B9003S) for 12hrs at 37°C in the dark on a rotating wheel. The reaction was run on 0.6% agarose 1xTAE gel pre-stained with SYBR Safe, the linear DNA band was excised, and the DNA was electro-eluted in 1xTAE. The eluate could be stored in the dark at 4C for a few days or at -80C for at least a few months.

### **Single-Molecule KEHRMIT Assay**

Immuno-Depleting Endogenous GINS: For each experiment endogenous GINS was immunodepleted in 3 rounds from 50 $\mu$ L NPE and in 2 rounds from 70 $\mu$ L HSS. For each round of NPE depletion 10 $\mu$ L Protein A Sepharose resin (PAS, GE Healthcare) was incubated with 50 $\mu$ g of affinity purified anti-GINS antibody at 4C overnight. For each round of HSS depletion, 14 $\mu$ L PAS resin was incubated with 70 $\mu$ g of antibody. The resin was pelleted in a swing-bucket rotor for 30sec at 2500g and washed twice with 1xTBS, once with 1xELB sucrose, twice with 1x ELB sucrose + 0.5M NaCl, and twice with 1xELB sucrose. Immuno-depletions were performed on a rotating wheel in the cold room for 45 min/each.

Flow Cell Assembly and DNA Tethering: Flow cells were assembled using 25x75x1mm slides (VWR Cat# 48300-025), double-sided tape (Grace Bio-Labs Cat# 620001), and PEG-ylated coverslips, as previously described (Yardimci et al., 2012a). 24x60mm No. 1.5 coverslips (VWR Cat# 16004-312) were PEG-ylated as described previously (Tanner et al., 2009) using a mixture of 10% Biotin-PEG-SVA and 90% M-PEG-SVA MW5000 (Laysan Bio). Linear DNA biotinylated at both ends ( $\lambda$  DNA or the 30.6kb DNA substrate with dual DPC lesions) was

stretched to ~90% of its contour length and immobilized onto the coverslip (Yardimci et al., 2012a). Immobilized DNA was stained with 200 nM SYTOX Green (Thermo Fisher Cat# S7020) and imaged using 488-nm laser excitation (details in the Microscopy section below). 20-50 fields of view (FOVs) near the flow cell inlet were selected and subsequently imaged during the replication experiment every 0.5-3min. The DNA stain was removed by washing the flow cell with 1xELB sucrose before any egg extracts were introduced.

Replication Reaction Mixture Assembly: After immuno-depleting HSS and NPE, the following mixtures were assembled. The ATP regeneration system (ARS) was assembled on ice by mixing 5 $\mu$ L 0.2M ATP (Sigma Cat# A-5394) with 10 $\mu$ L 1M Phosphocreatine (Sigma Cat# P-6502) and 0.5 $\mu$ L 5 mg/mL Creatine Phosphokinase (Sigma Cat# C-3755).  $\Delta$ HSS-NPE Mix was assembled at room temperature by mixing 31 $\mu$ L GINS-depleted NPE with 31 $\mu$ L GINS-depleted HSS, and incubated at room temperature for 5min to inactivate Cdt1. The Licensing Mix was assembled by supplementing 20 $\mu$ L of GINS-depleted HSS with 2 $\mu$ L of 30-bp long dsDNA carrier (300ng/ $\mu$ L stock)(Loveland et al., 2012; Yardimci et al., 2012a) and 0.7 $\mu$ L ARS, then incubated at room temperature for 5min. The Replication Initiation Mix was assembled by adding 3 $\mu$ L pBlueScript carrier plasmid DNA (200ng/ $\mu$ L stock) (Lebofsky et al., 2011), 1 $\mu$ L ARS, 4 $\mu$ L 1xELB Sucrose, and 1 $\mu$ L rGINS<sup>AF647</sup> (0.3-1.0 mg/mL stock) to 18 $\mu$ L of  $\Delta$ HSS-NPE Mix, then incubated at room temperature for 5min. The Replication Elongation Mix was assembled by supplementing 40 $\mu$ L of  $\Delta$ HSS-NPE Mix with 7 $\mu$ L pBlueScript carrier plasmid DNA (200ng/ $\mu$ L stock), 2 $\mu$ L ARS, 11 $\mu$ L 1xELB sucrose, and, optionally 1-2 $\mu$ L of Fen1<sup>mKikGR</sup> (100 $\mu$ M stock), and incubated at room-temperature for 5min.

DNA Replication and Imaging: After the DNA was tethered as described above, replication origins were licensed by flowing 15 $\mu$ L of Licensing Mix into the flow cell at 10 $\mu$ L/min, and incubating for 2-5min. Replication origins were fired by flowing 20 $\mu$ L of Replication

Initiation Mix at 10 $\mu$ L/min, and incubating for 2-5min. Excess free rGINS<sup>AF647</sup> was washed away by flowing 55 $\mu$ L of Replication Elongation Mix at 10 $\mu$ L/min. 2-3 minutes after starting the wash AF568 (for DPC experiments) or mKikGR (for  $\lambda$  DNA experiments) and AF647 were imaged every 0.5-3min for 1-3hrs. Since the PCA/PCD oxygen scavenging system inhibited DNA replication (data not shown), and the glucose oxidase/catalase oxygen scavenging system is incompatible with experiments in cell extracts (Aitken et al., 2008) oxygen scavengers were omitted and stroboscopic imaging was employed to limit photobleaching.

Microscopy: Single-molecule data was collected at the Nikon Imaging Center at Harvard Medical School on a Nikon Ti motorized inverted microscope (“Tobias”) equipped with CFI Apochromat TIRF NA1.49 oil immersion objective with 100X magnification, the Perfect Focus System for maintenance of focus over time, a Nikon TIRF illuminator, an Agilent MLC400B laser launch with 405 nm (20mW), 488 nm (50mW), 561 nm (50mW), and 647 nm (125mW) (power measured at fiber optic). Images were acquired using a ZT405/488/561/647rpc dichroic (Chroma) with an Andor DU-897 EM-CCD camera controlled by NIS Elements software.

SYTOX Green fluorescence was excited with the 488 nm laser (<0.1mW measured at the objective) for 100ms and collected with an ET525/50m emission filter (Chroma). AF568 fluorescence was excited with the 561 nm laser (0.5-1.0mW) for 100 ms and collected with an ET600/50m emission filter (Chroma). AF647 fluorescence was excited with the 647 nm laser (0.5-1.0mW) for 100 ms and collected with an ET700/75m emission filter (Chroma). Fen1<sup>mKikGR</sup> was photo-switched with the 405 nm laser (0.5-1.0 mW) for 100ms, allowed to diffuse for 400ms, then mKikGR fluorescence was excited with the 561 nm laser (0.5-1.0 mW) for 100ms and collected with a ET600/50m emission filter (Chroma) (Loveland et al., 2012).

For time-lapse experiments, images were collected every 0.5-3 min (depending on the experiment) at 20-50 different fields of view (FOVs). Multiple FOV positions were collected

using a Prior Proscan II linear-encoded motorized stage. Movie frames for each FOV were aligned in ImageJ using the Image Stabilizer Plugin (Li, 2008).

### KEHRMIT Data Analysis

A typical KEHRMIT experiment generated a movie containing several fields of view (FOV), and each FOV initially contained ~100 double-tethered DNA molecules of the correct size (48.5kb  $\lambda$  DNA or 30.6kb DPC substrate extended to ~90% of their respective contour lengths). A significant portion of DNA molecules ruptured when egg extract mixtures were introduced into the flow cell. DNA molecules that were tethered too close to each other aggregated in egg extracts and were omitted from analysis. Molecules where multiple replication origins fired close to each other were also discarded. Only replication origins that gave rise to two labeled CMG molecules were included in the analysis. Active CMG molecules were detected by generating a maximum-intensity z-projection of the CMG<sup>AF647</sup> channel where translocating CMG molecules appeared as a contiguous bright trail. Regions of interest (ROIs) corresponding to active helicases were hand-selected, automatically cropped, rotated, and individual frames were stacked to generate kymograms. The fluorescent spot image corresponding to individual CMG molecules was fitted by a 2D Gaussian and its position was determined to sub-pixel accuracy. Translocation velocity was computed by linear fitting of CMG position versus time to a straight line. Processivity was measured as the distance traveled by CMG from the beginning of the experiment until the AF647 signal disappeared due to photobleaching, DNA tether rupture, or CMG reaching the end of the DNA template. When analyzing data from aphidicolin uncoupling experiments, it was taken into account that at a low force the length of RPA-bound ssDNA is essentially the same as that of dsDNA (Lewis et al., 2017). In experiments with the 30.6kb DNA-DPC substrate, only DNA molecules containing two labeled DPCs at the expected distance were included in the analysis. Furthermore,

DPC<sup>Lead</sup> and DPC<sup>Lag</sup> encounters were classified according to the location of the replication initiation event relative to the two lesions as illustrated in Figure 6B. CMG pauses at the DPC were identified as segments of the helicase trajectory where the CMG position was within 1px (160 nm) of the DPC. Unambiguous DPC bypass events (BID) were defined as CMG encounters with a DPC<sup>Lead</sup> or DPC<sup>Lag</sup> where both approach and departure could be unambiguously detected (at least 3 timepoints for each) and the corresponding velocities could be reliably measured. DD+ events were defined as CMG encounters with a DPC<sup>Lead</sup> or DPC<sup>Lag</sup> where the DPC<sup>AF568</sup> signal disappeared but the CMG<sup>AF647</sup> signal persisted, and CMG travelled at least 1px from the original site of the DPC. Conversely, DD- events were defined as CMG encounters with a DPC<sup>Lead</sup> or DPC<sup>Lag</sup> where the DPC<sup>AF568</sup> signal disappeared, the CMG<sup>AF647</sup> signal persisted, but CMG travelled less than 1px from the site of the DPC. B+M events were defined as CMG-DPC<sup>Lag</sup> encounters where both CMG<sup>AF647</sup> and DPC<sup>AF568</sup> signals persisted and both CMG and DPC travelled more than 3px from the initial DPC<sup>Lag</sup> position. Since data was acquired at 1min/frame, pause durations and DPC lifetimes are reported as integers in increments of 1min. Error-bars for mean or median values corresponding to distributions were estimated as 95% confidence intervals via bootstrapping.

### KEHRMIT Assay Strengths and Limitations

The KEHRMIT assay offers a few key advantages over fiber analysis – the most common assay used to measure the average speed of replication forks, and PhADE – a real-time assay for imaging the growth of nascent DNA tracts (PhotoActivation, Diffusion and Excitation). (i) KEHRMIT directly monitors CMG dynamics as opposed to DNA synthesis. (ii) KEHRMIT provides temporal information that reveals changes in fork speed or transient helicase pausing. (iii) KEHRMIT has a higher spatial resolution than either DNA combing or PhADE because the position of the CMG helicase on DNA can be determined with sub-pixel accuracy. However,

KEHRMIT is incompatible with simultaneous imaging of SYTOX-stained DNA because at the high protein concentration present in *Xenopus* egg extracts cross-links SYTOX-stained DNA to the surface of PEG-functionalized glass coverslips. Instead, the DNA molecules can be stained and imaged after they are immobilized, and de-stained prior to adding egg extracts to the flow cell. Optionally, DNA can also be SYTOX-stained and imaged after replication in egg extracts and stringent washing with SDS-containing buffer (Yardimci et al., 2012a), but some double-tethered DNA molecules break during replication and subsequently cannot be visualized using SYTOX. In the labeling scheme presented here, dual-color CMG<sup>AF647</sup> and DPC<sup>AF568</sup> imaging is incompatible with simultaneous PhADE imaging of Fen1<sup>mKikGR</sup> bound to nascent DNA (Loveland et al., 2012) because the absorbance/emission spectra of AF568 and the photo-switched form of mKikGR overlap. Consequently, the DPC<sup>AF568</sup> signal could not be distinguished from that of Fen1<sup>mKikGR</sup>. In addition, the use of Fen1<sup>mKikGR</sup> at very high concentration (1-3  $\mu$ M) to image nascent DNA synthesis by PhADE precludes the concomitant use of any green fluorophores (such as AF488) because of overlapping absorbance/emission spectra with the green form of mKikGR (Habuchi et al., 2008).

## Supplemental Figure Legends

**Figure S1.** Related to Figure 1. **(A)** Schematic showing trapping of M.HpaII on a plasmid containing a fluorinated M.HpaII recognition site. **(B)** Schematic of the two replication-coupled DPC proteolysis pathways in *Xenopus* egg extracts (Larsen et al., *submitted*). **(C)** Mock-depleted and SPRTN-depleted egg extracts were blotted using SPRTN and Mcm10 (loading control) antibodies. **(D)** pmeDPC<sup>2xLead</sup> was replicated in the indicated egg extracts. At different times, plasmid was recovered under stringent conditions, the DNA digested, and the released proteins subjected to immunoblot analysis with M.HpaII antibody. **(E)** pmeDPC<sup>Lead</sup> was replicated in SPRTN-depleted extract that was also mock or REV1-depleted containing [ $\alpha$ -<sup>32</sup>P]dATP. Samples were processed and analyzed as in Figure 1C. **(F)** Alternative models to explain the disappearance of the CMG footprint at stable DPCs: CMG dissociation (i) or CMG bypass (ii). **(G)** Model of CMG dynamics on pmeDPC<sup>2xLead</sup>. After CMGs bypass the two-leading strand DPCs, CMGs converge, as seen during replication termination, whereupon they are ubiquitinated (probably by CRL2<sup>Lrr1</sup> (Dewar et al., 2017)), and unloaded by p97. **(H)** pDPC<sup>Lead</sup> was replicated in undepleted extract containing [ $\alpha$ -<sup>32</sup>P]dATP and supplemented with buffer or 100  $\mu$ M Cdc7i (PHA767491) at zero or ten minutes after NPE extract addition, which initiates replication, and analyzed as in Figure 1C. **(I)** A serial dilution of mock-depleted egg extract was analyzed alongside FancM-depleted egg extracts via blotting with FancM antibody. **(J)** pDPC<sup>2xLead</sup> was replicated in SPRTN-depleted extract that was also mock or FancM-depleted and supplemented with [ $\alpha$ -<sup>32</sup>P]dATP. At different times, DNA was recovered and nicked with Nb. BsmI, separated on a denaturing polyacrylamide gel, and visualized by autoradiography. **(K)** Upper panel: pDPC<sup>2xLead</sup> was replicated in undepleted extract containing [ $\alpha$ -<sup>32</sup>P]dATP and supplemented with either buffer or ATRi. Samples were processed and analyzed as in Figure S1J. Lower panel: same extracts without addition of [ $\alpha$ -<sup>32</sup>P]dATP were

replicated and reaction samples were separated by SDS-PAGE and blotted with the indicated antibodies.

**Figure S2.** Related to Figure 2. Proposed action of a 5' to 3' helicase (pink) on four different substrates (i-iv).

**Figure S3.** Related to Figure 3. **(A)** Egg extracts contain multiple RTEL1 isoforms, as seen in lane 1 and Figure 3B, lane 1. To distinguish them, we depleted egg extract with an antibody raised against an N-terminal fragment of RTEL1 ( $\alpha$ -RTEL1-N, lane 2; used in all experiments except lane 3 of this panel) or an antibody raised against a C-terminal peptide ( $\alpha$ -RTEL1-C, lane 3), and blotted with  $\alpha$ -RTEL1-N or ORC2 (loading control) antibodies. Unlike  $\alpha$ -RTEL1-N,  $\alpha$ -RTEL1-C depleted only the largest RTEL1 isoform, consistent with the presence of multiple isoforms (as seen in mice (Ding et al., 2004)), only the largest of which has the C-terminal extension against which the antibody was raised. Depletion of extracts with  $\alpha$ -RTEL1-C antibody (lane 3) had no effect on CMG bypass (data not shown), demonstrating that the shorter isoforms were sufficient to perform this function. **(B)** Incorporation of [ $\alpha$ -<sup>32</sup>P]dATP during pmeDPC<sup>Lead</sup> replication in mock-depleted or RTEL1-depleted extract was quantified and graphed. The mean of five experiments is shown. Error bars represent the standard deviation. **(C)** Coomassie blue-stained SDS-PAGE of purified RTEL1 wild-type and RTEL1-K48R. The RTEL1 and co-purifying GST-tag bands are indicated. **(D)** pmeDPC<sup>Lead</sup>, pmeDPC<sup>Lag/Lead</sup>, and pmeDPC<sup>Lag/Lead-Bubble</sup> were replicated in the presence of [ $\alpha$ -<sup>32</sup>P]dATP in SPRTN-depleted egg extracts that were also mock-depleted or RTEL1-depleted and analyzed as in Figure S1J. The mean of three experiments is quantified. Error bars represent the standard deviation. **(E)** Quantification of CMG bypass in Figure 3D. **(F)** DNA samples from Figure 3E were digested

with AflIII, separated on a non-denaturing agarose gel, and linear products were quantified. The mean of three experiments is graphed. Error bars represent the standard deviation.

**Figure S4.** Related to Figure 4. **(A)** pDPC<sup>2xLead</sup> was replicated in mock-depleted or RTEL1-depleted egg extracts. At different times, plasmid-associated proteins were recovered under non-stringent conditions and blotted with the indicated antibodies. **(B)** Mock-depleted and RTEL1-depleted extracts used in Figure 4E were supplemented with [ $\alpha$ -<sup>32</sup>P]dATP and used to replicate pDPC<sup>2xLead</sup>. DNA samples were separated on a native agarose gel and subjected to autoradiography. The gel shows that in the absence of RTEL1, replication products accumulated as slow mobility intermediates instead of undergoing dissolution into monomeric open circular (OC) and supercoiled (SC) plasmids, reflecting a defect in CMG bypass and lack of DNA unwinding of the 165 bp that separates the DPCs (see cartoon). **(C)** pDPC<sup>ssDNA</sup> was incubated directly in mock-depleted or RTEL1-depleted NPE without first licensing in HSS, which prevents replication initiation due to the high concentration of Geminin in NPE (Arias and Walter, 2005). Chromatin was isolated by the stringent pull-down procedure described in Figure 4A and analyzed for M.HpaII levels. RTEL1 depletion had no effect on the rate of M.HpaII destruction. **(D)** Same as in (C) except that M.HpaII conjugated to the gapped plasmid was methylated to inhibit the proteasome pathway. Short and long (larger excerpt) exposures of the same blot are shown. The result shows that in the setting of ssDNA, the SPRTN-specific product was generated at the same rate whether or not RTEL1 was present

**Figure S5.** Related to Figure 5. **(A-B)** pmeDPC<sup>2xLead</sup> was replicated in mock-depleted or GINS-depleted egg extracts containing [<sup>32</sup>P]dATP and supplemented with buffer or rGINS<sup>AF647</sup>. At the indicated times, DNA was recovered, resolved on a native agarose gel (A) or a sequencing gel

(B), and visualized by autoradiography. Endogenous GINS depletion abolished and recombinant GINS<sup>AF647</sup> fully rescued DNA replication (A). rGINS<sup>AF647</sup> also supported loss of the CMG footprint (B). (C) The efficiency of DPC bypass by CMG from panel B and two additional experiments was quantified as described in Figure 2B and graphed. (D) A serial dilution of mock-depleted and GINS-depleted NPE was supplemented with buffer, 300 nM (1x) or 600 nM (2x) AF647-labeled rGINS, or 300 nM (1x) unlabeled rGINS, and analyzed by western blotting with antibodies against the Psf1 subunit of GINS. (E) Integrated fluorescence intensity traces for individual CMG molecules traveling along  $\lambda$  DNA illustrated that AF647 photobleached in a single step. (F) Kymogram of a replication bubble (as in Figure 5C) illustrating that the replication fork continues to travel (blue) after AF647 (green) photobleaching (arrow).

**Figure S6.** Related to Figure 6. (A) Example of automated analysis of a DPC<sup>Lead</sup> bypass event. (Left) Kymogram of the CMG-DPC<sup>Lead</sup> encounter. (Middle) CMG and DPC positions were determined by fitting the centroid of the corresponding fluorescent signal. (Right) Plot of CMG-DPC distance. Approach (green), pause (red), and departure (blue) phases were detected by an automated algorithm (See methods). (B) Examples of BID, DD+, DD-, CD, and DT events. (C) Photobleaching kinetics for DPC<sup>AF568</sup> and GINS<sup>AF647</sup> (200 molecules were analyzed in each case).  $T_{1/2}$  denotes the half-life extracted from the exponential decay fit (solid lines) to the raw data (dots). The experiment was conducted in egg extract with DPC<sup>AF568</sup> and GINS<sup>AF647</sup> non-specifically bound to the glass coverslip using the same laser power and frame rate as experiments described in Figure 6. These data suggest that AF647 photobleaching is a major contributor to CD events. Although AF568 photobleaching contributes to DD+/- events for stabilized DPCs, it plays only a minor role in DD+/- events for degradable DPCs. (D) Quantification of three different classes of CMG-DPC<sup>Lag</sup> encounters from two sets of

experiments: (i) Bypass of intact DPC (BID), representing unambiguous bypass events; (ii) CMG bypassed the DPC position followed by DPC mobilization due to sister chromatid separation (B+M). (iii) DPC disappeared first, followed by CMG departure from the pause site (DD+). These are probably bypass events where the DPC was degraded before CMG departure. (E) Two examples of B+M events at meDPC<sup>Lag</sup> in SPRTN-depleted extract. (F) Model of how B+M events result from sister chromatid separation when the outward-moving CMG reaches the end of the DNA substrate. (G) Histograms of meDPC lifetime in mock-depleted extract in the absence of replication (+geminin control to block origin firing) versus meDPC<sup>Lead</sup> in SPRTN-depleted extracts and nonmethylated DPC<sup>Lead</sup> in mock-depleted extract, both in the presence of replication. In all cases, DPC lifetime was measured from the beginning of the experiment. The peak at 90-100 min corresponds to DPC<sup>AF568</sup> molecules that survived the entire 100-min experiment. Blue lines and gray boxes correspond to the mean and the 95% CI. (H) Replication origins firing in extracts supplemented with vehicle (left) or 150  $\mu$ M aphidicolin (right). CMG and nascent DNA signals are shown in green and blue respectively (same as Figure 5C). The absence of blue signal in the +Aph. experiment confirms the inhibition of DNA synthesis. (I) Beeswarm plot of CMG processivity in the presence of aphidicolin. Blue lines and gray boxes correspond to the mean and the 95% CI. (J) Beeswarm plot of the time needed to bypass methylated DPC<sup>Lead</sup> in SPRTN-depleted extract versus nonmethylated DPC<sup>Lead</sup> in undepleted extract. Blue lines and gray boxes as in (I).

**Figure S7.** Related to Figure 6. (A) pLacO<sub>32</sub> was pre-incubated with LacR and replicated in mock-depleted or SPRTN-depleted egg extracts containing [ $\alpha$ -<sup>32</sup>P]dATP and supplemented with DMSO or MG262. At the indicated times, DNA was recovered, digested with the single

cutter XmnI, resolved by native agarose gel electrophoresis, and visualized by autoradiography. Accumulation of the linear species is quantified. **(B)** Bypass model in which CMG denatures the DPC and threads the resulting polypeptide chains through the central channel of the MCM2-7. **(C)** Bypass model in which the MCM2-7 ring transiently opens, possibly due to dissociation of GINS and/or CDC45 (not shown), allowing the helicase to translocate or be towed (not shown) past the DPC. **(D)** Model for template switching at a DPC. If CMG bypasses the DPC but TLS fails, the leading strand anneals to the nascent lagging strand. After extension of the leading strand (blue arrow), it undergoes dissolution and re-anneals to the leading strand template, thereby bypassing the adduct.

# Figure 1

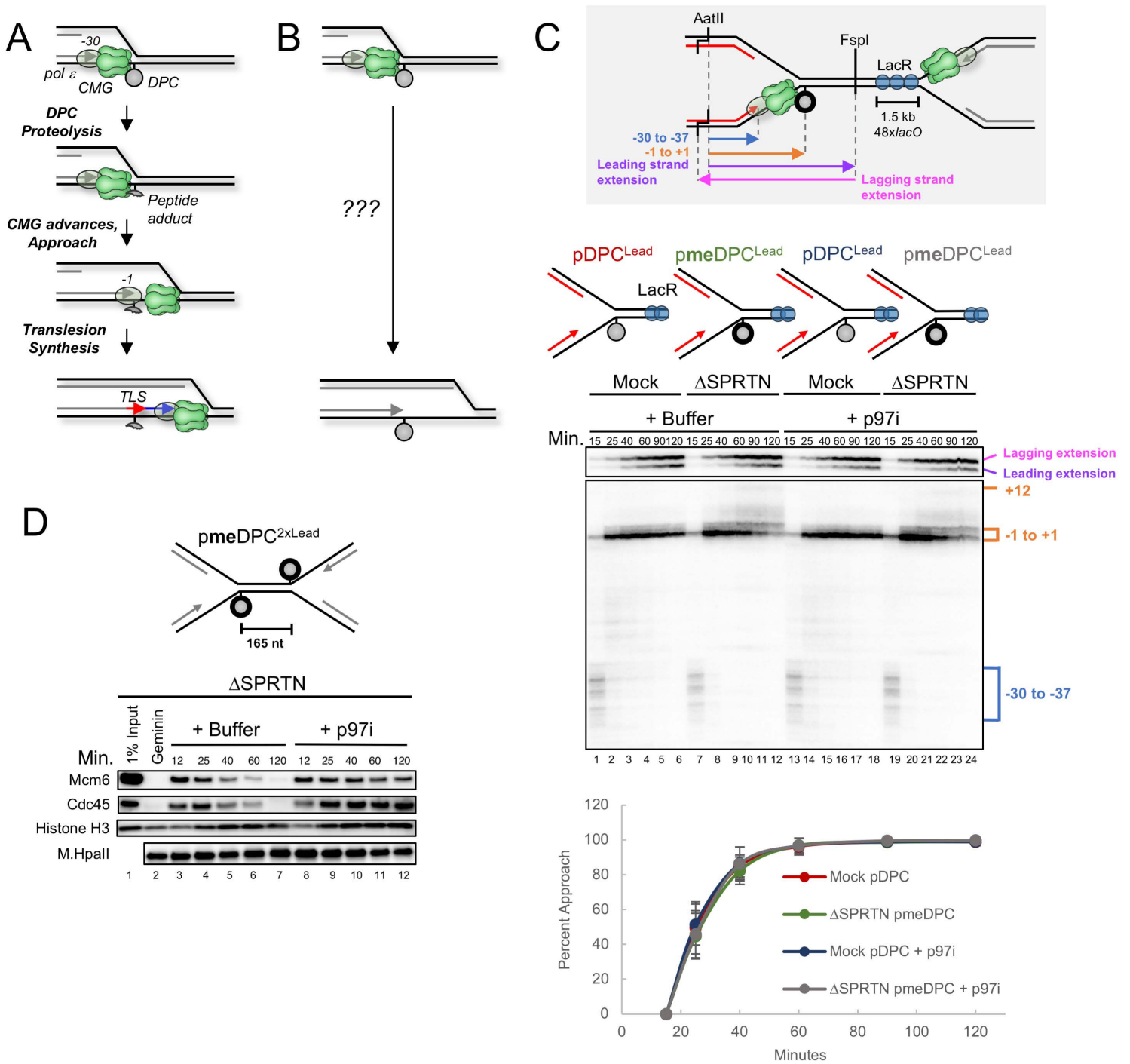
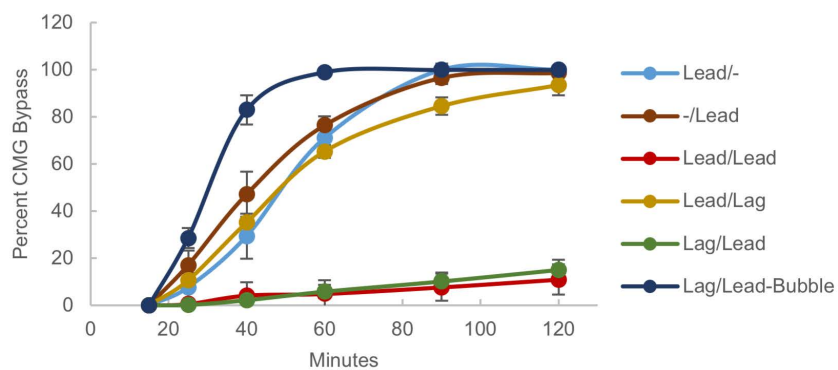
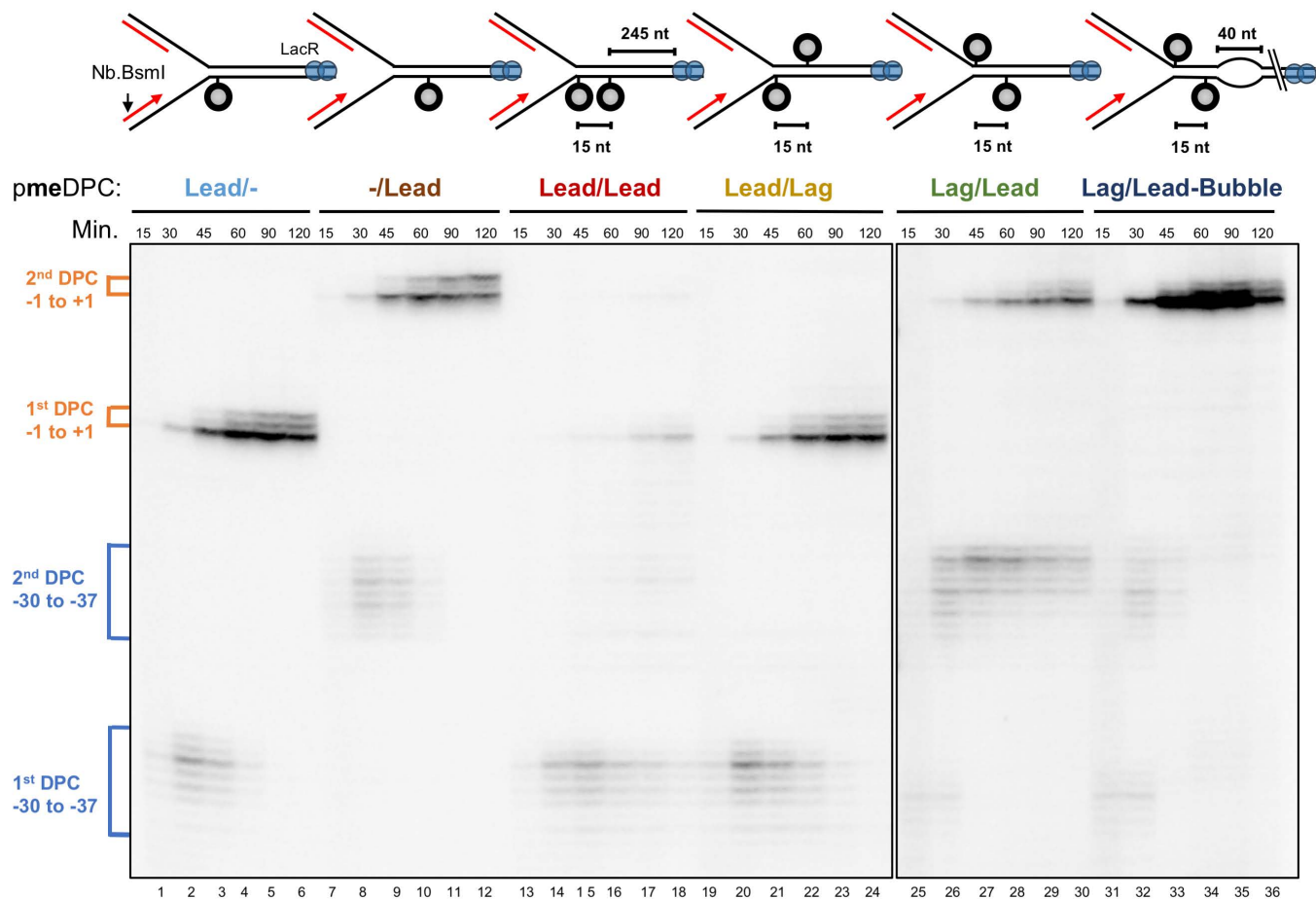


Figure 2



# Figure 3

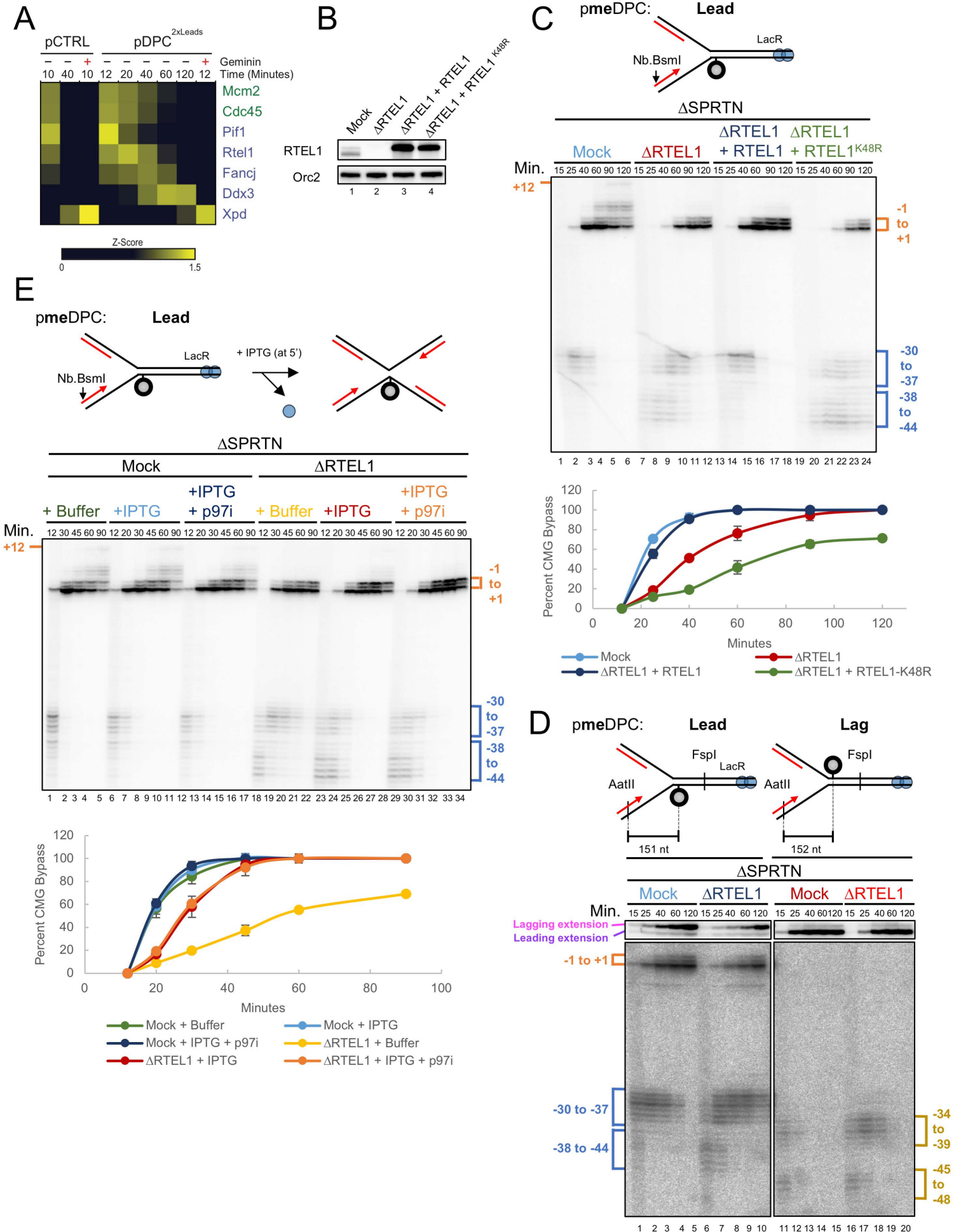


Figure 4

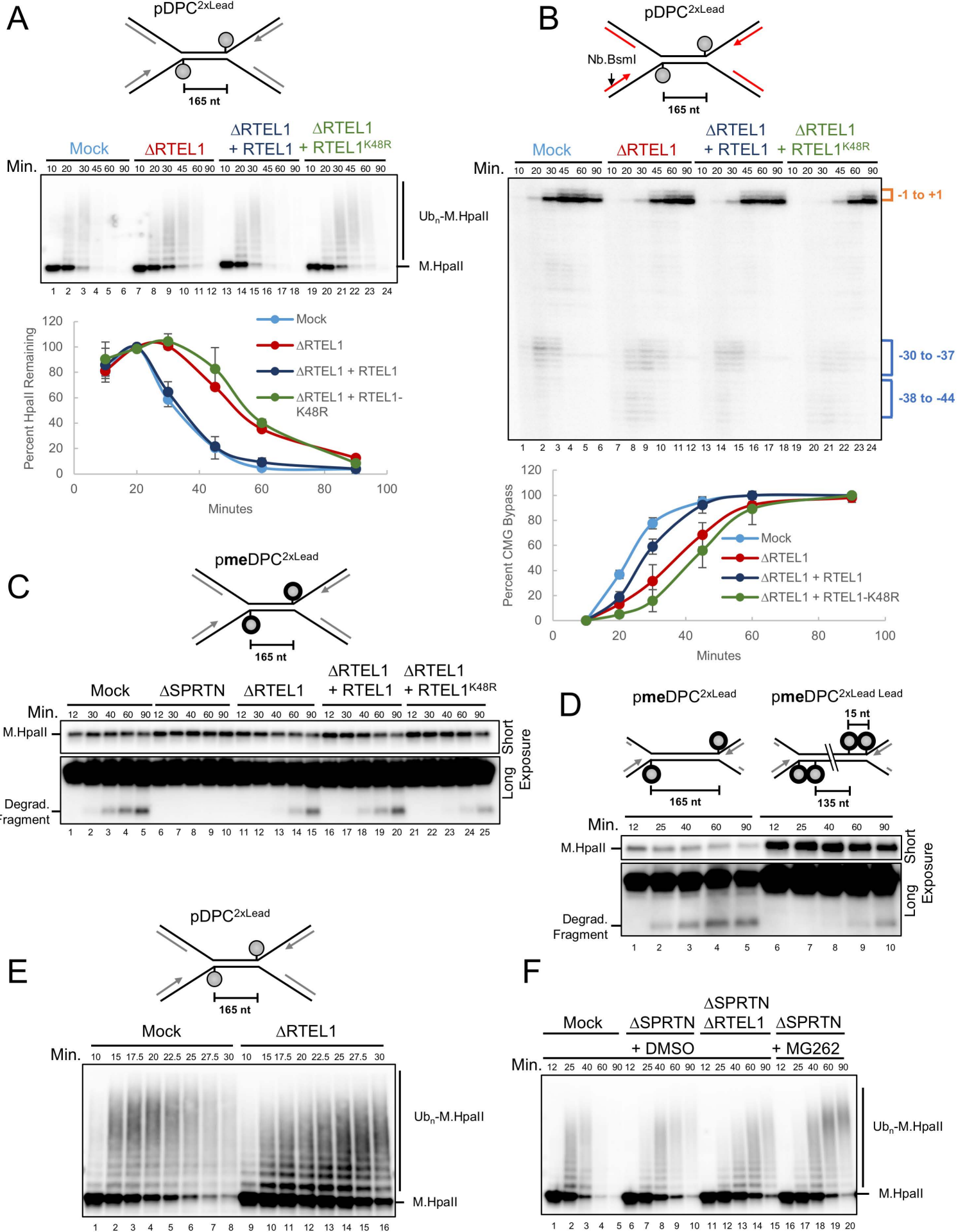


Figure 5

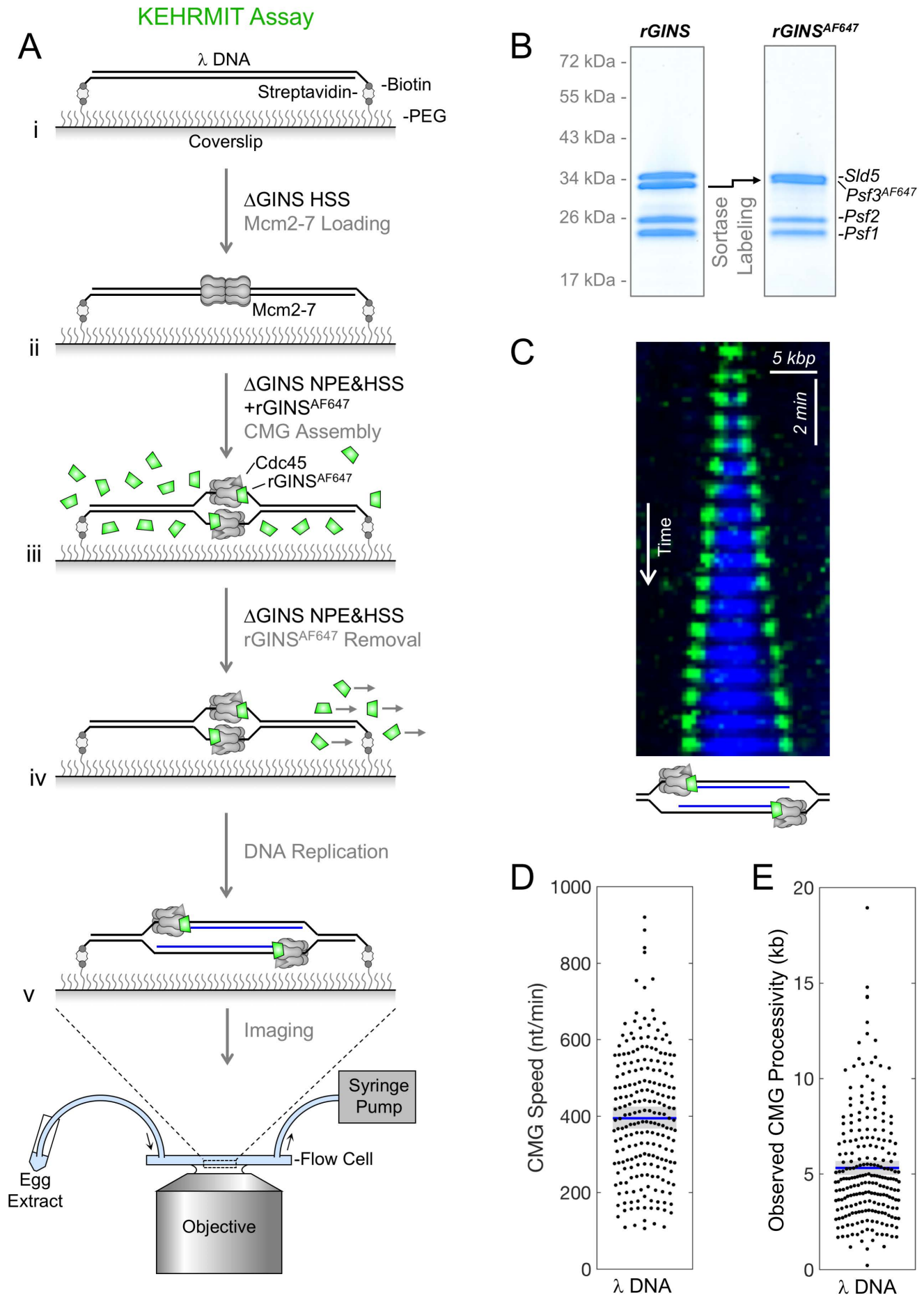


Figure 6

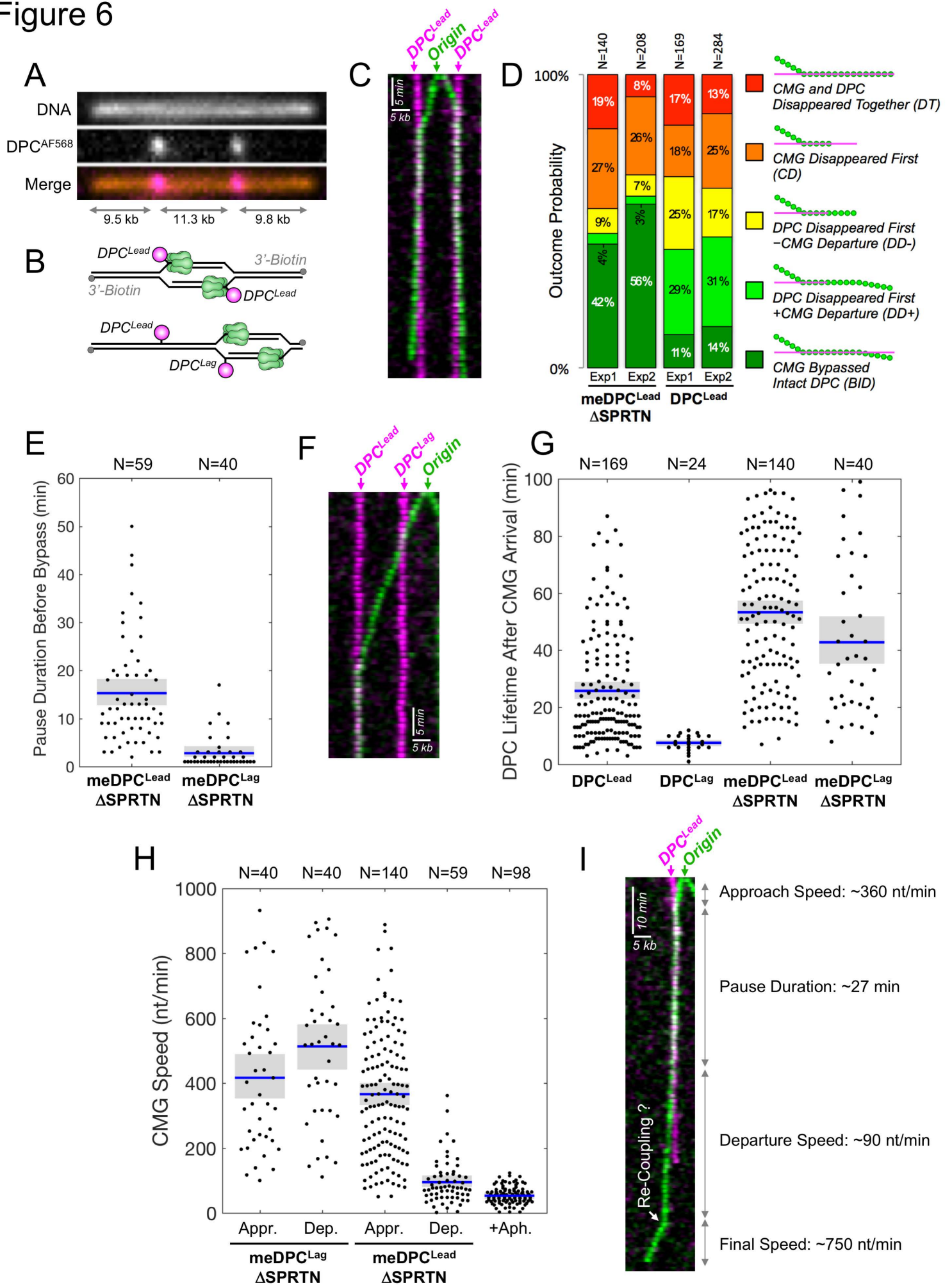
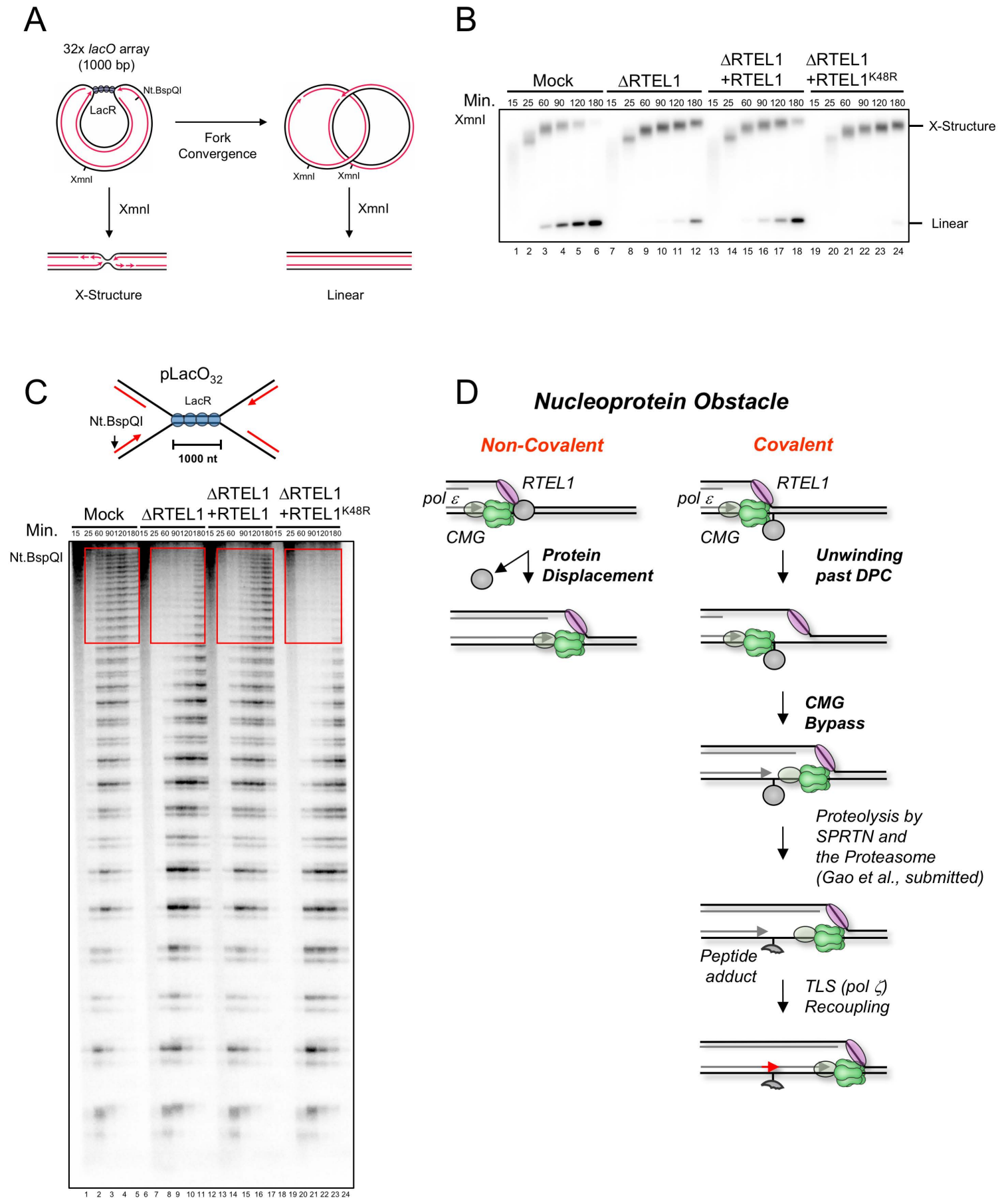
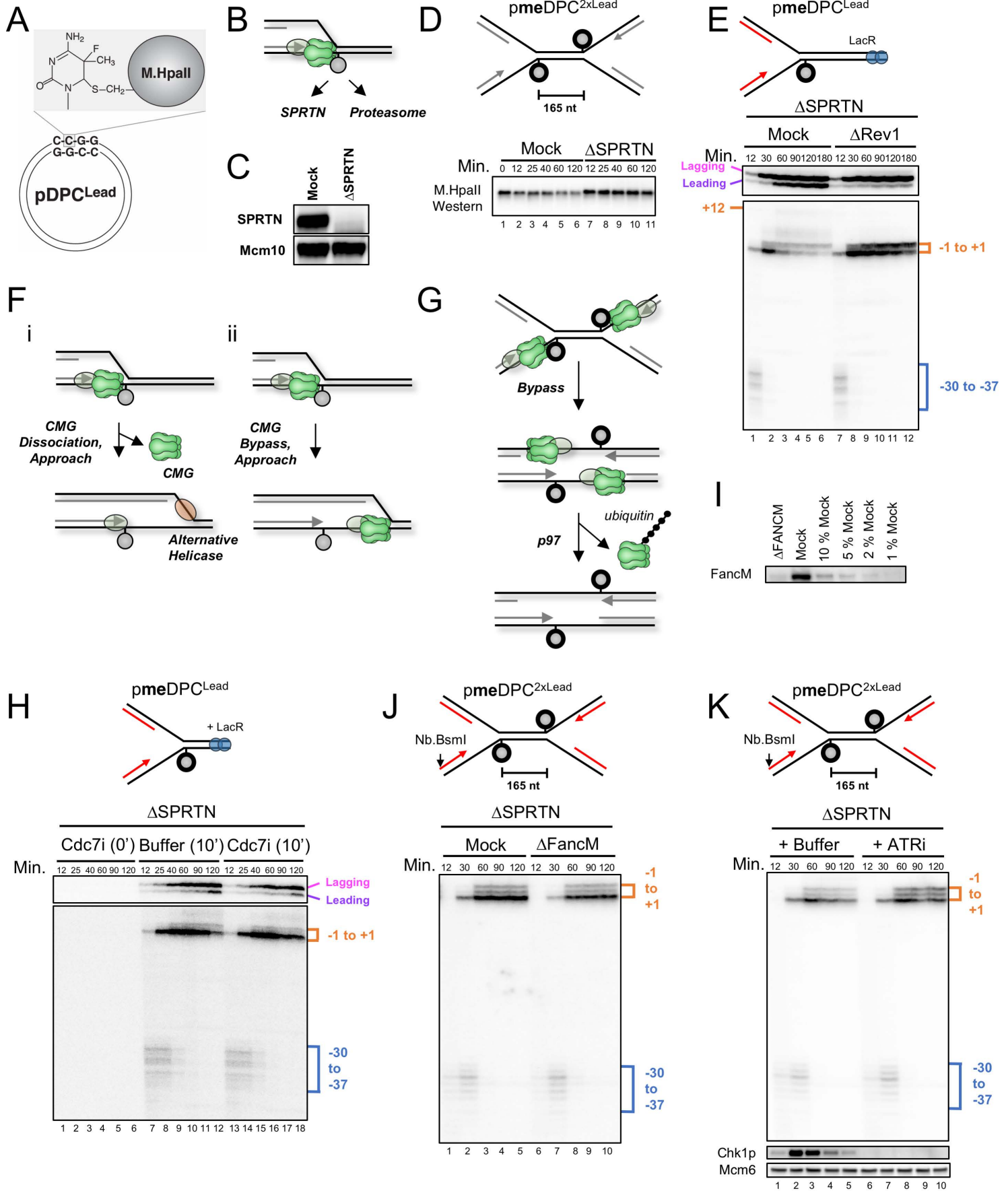


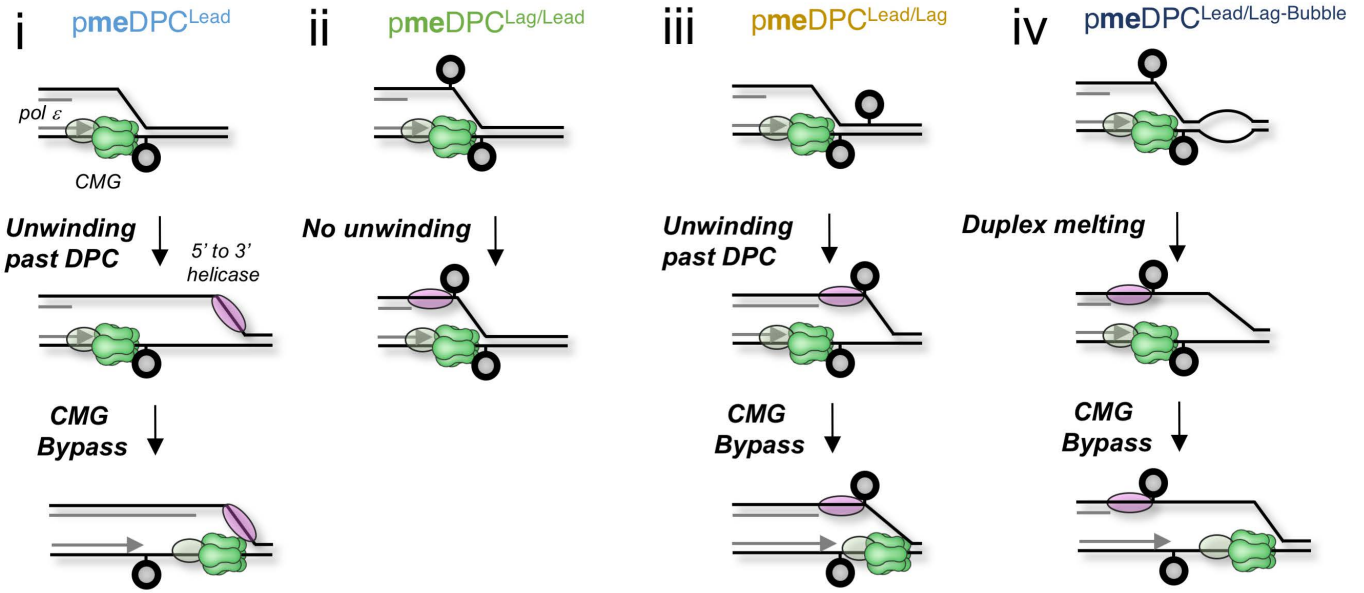
Figure 7



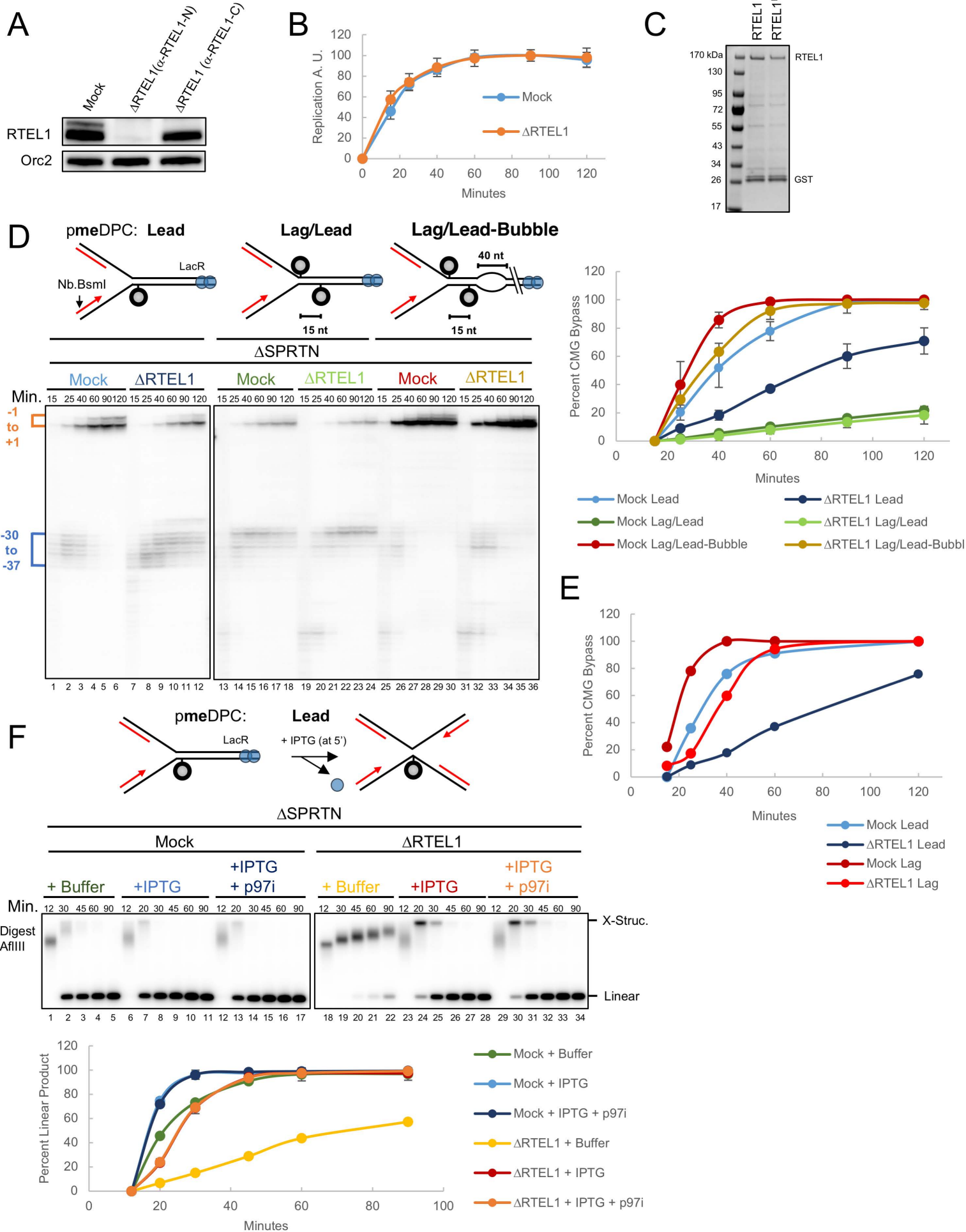
# Supp. Figure 1



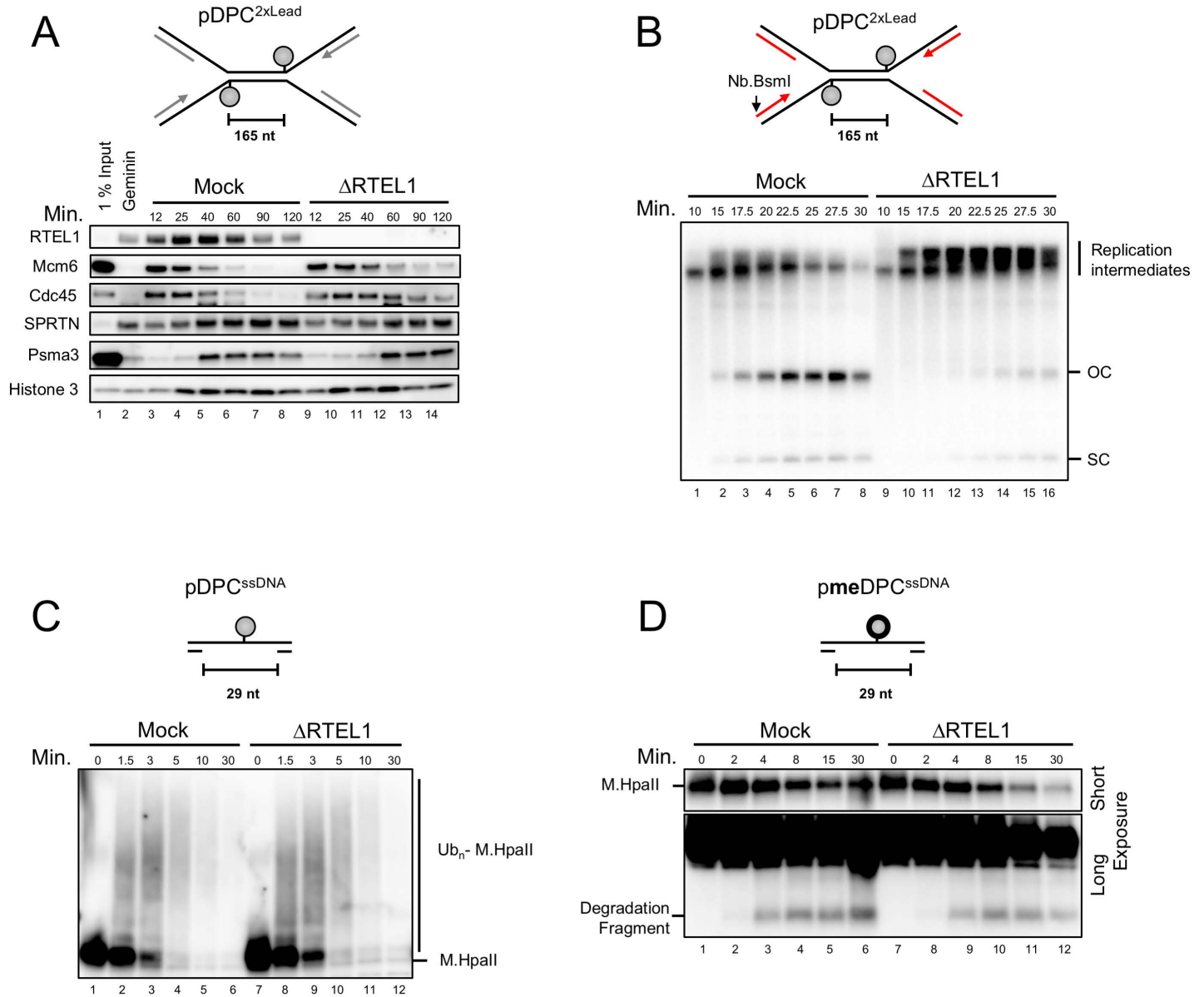
# Supp. Figure 2



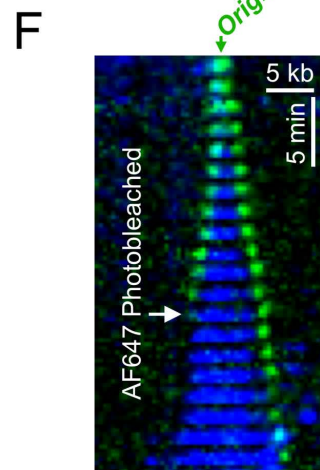
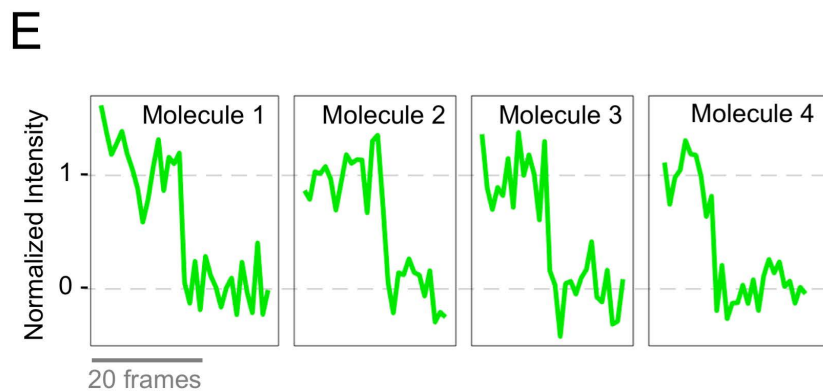
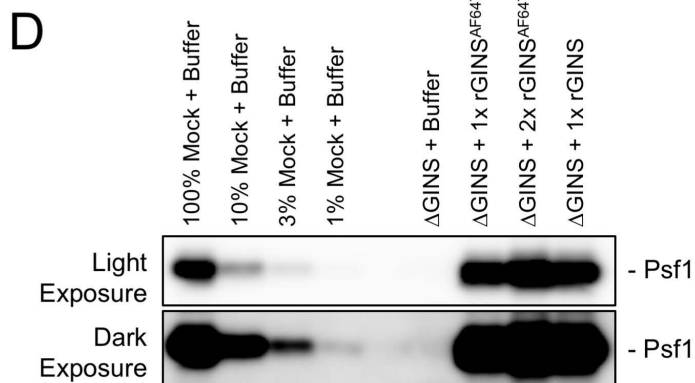
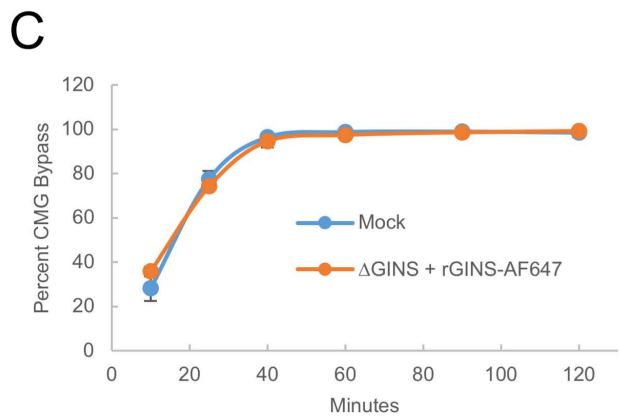
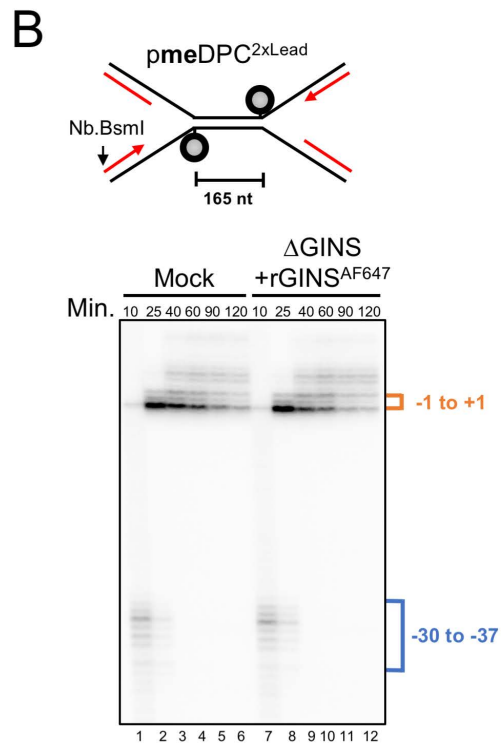
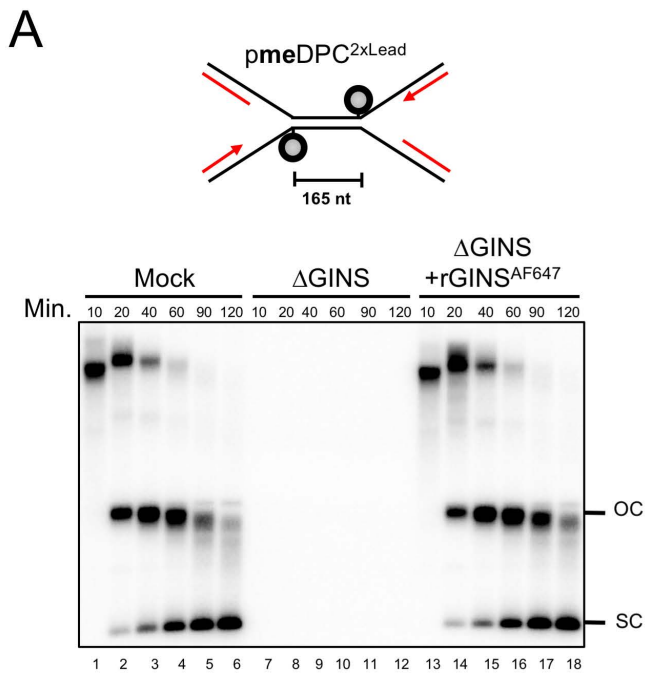
# Supp. Figure 3



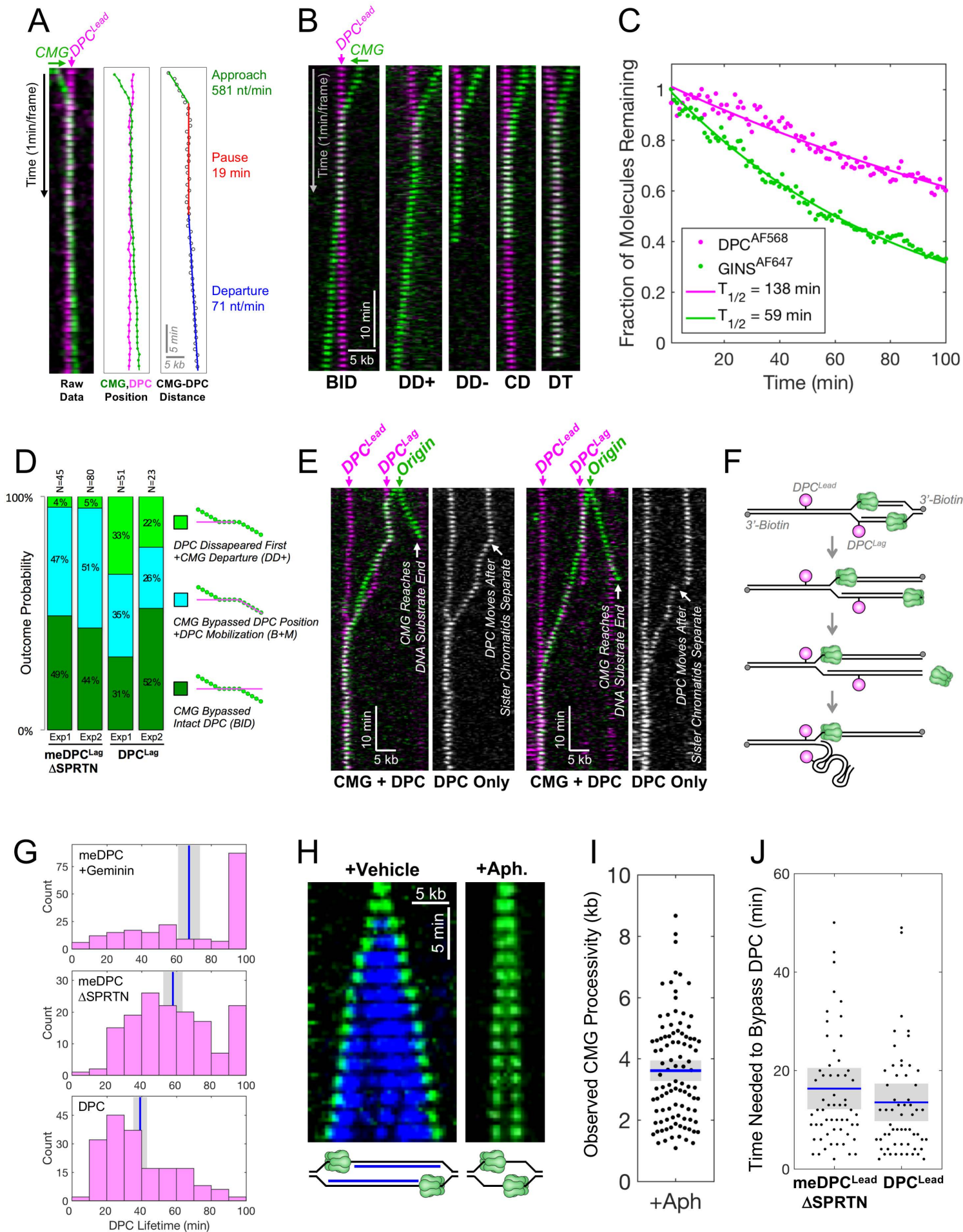
# Supp. Figure 4



# Supp. Figure 5



# Supp. Figure 6



# Supp. Figure 7

